A mesoscale model study of summertime atmospheric circulations in the north polar region of Mars

Daniel Tyler Jr. and Jeffrey R. Barnes
College of Oceanic and Atmospheric Sciences, Oregon State University, Corvallis, Oregon, USA

Received 3 September 2004; revised 27 March 2005; accepted 14 April 2005; published 29 June 2005.

[1] The Oregon State University Mars MM5 was used in a comprehensive high-resolution study of northern polar summertime circulations. Three simulations (L_s = 120, L_s = 135, and L_s = 150) characterize the changing circulation. The atmosphere is dry, and model dynamics are hydrostatic. A modified TES thermal inertia map provides a realistic simulation of the polar thermal environment. The highest-resolution nest (18 km) resolves complex flows near the cap; zonal-mean easterlies (~10 m/s) and zonal-mean katabatic winds (~5 m/s) near the surface are relatively steady during this study. Katabatic flows are shallow (~300 m); the easterlies are deeper (~1.5 km). Transient eddies are very important within the first scale height; they are excited by mechanisms, and at locations, that change dramatically during this short study period. At L_s = 120 they form along the residual cap edge with a zonal wave number one structure, producing strong excursion winds (10–15 m/s) that blow consistently across the cap. By L_s = 135, strong eddies are seen to form on the northern slopes of Alba Patera and Tharsis. These eddies are quite suggestive of the large annular cloud structures seen in Hubble Space Telescope and Mars Orbital Camera imagery at this location and season and can traverse the high latitudes to reach the residual cap before dissipating. Eddies in the earlier two simulations appear to be primarily excited by energetic flows near the surface. By L_s = 150 an early fall polar jet causes strong winter-like baroclinic eddies to develop. The transient eddies found in this study are probably important in the water cycle of the northern residual cap.

Citation: Tyler, D., Jr., and J. R. Barnes (2005), A mesoscale model study of summertime atmospheric circulations in the north polar region of Mars, *J. Geophys. Res.*, *110*, E06007, doi:10.1029/2004JE002356.

1. Introduction

[2] Mesoscale models of the Martian atmosphere have become important tools in efforts to understand the Martian climate system. Increasingly, these models are being used in studies of climatologically important regional and smaller-scale circulations in the Martian atmosphere [e.g., *Rafkin et al.*, 2002; *Toigo et al.*, 2002; *Tyler et al.*, 2002; *Toigo et al.*, 2003; *Michaels and Rafkin*, 2004]. Atmospheric dynamics are very important in the climate of the northern polar region; transient circulations in the atmosphere influence the formation and recession of the seasonal carbon dioxide frosts and play an important role in the annual water cycle of the North Pole Residual Cap (NPRC). Mesoscale circulations will be prominent near the NPRC due to the sharp changes in topography, albedo and thermal inertia that exist on relatively small spatial scales; strong flows will be excited because of the thermal contrasts that form in response to gradients in these surface properties.

0148-0227/05/2004JE002356$09.00

[3] In this study we use a mesoscale model with a realistic representation of the polar thermal environment, thus we resolve and characterize mesoscale circulations in the polar atmosphere. We examine a relatively narrow range of solar longitude (L_s), from L_s = 120 to L_s = 150, centered on the mean L_s of summer, defined terrestrially as the period between summer solstice (L_s = 90) and fall equinox (L_s = 180). On Mars summer should probably not be defined in the terrestrial way since there are no oceans to cause the warmest temperatures to significantly lag the date of the most poleward subsolar latitude (L_s = 90). By L_s = 150 the weather in the northern polar region is no longer summer-like. These simulations provide new information about Martian polar circulations at intermediate and higher resolution and can be used to help guide future modeling efforts.

[4] General Circulation Models (GCMs) are valuable tools for investigating the complex relationships between the numerous physical processes at work in the polar atmosphere. *Pollack et al.* [1990] used an early version of the NASA Ames Mars GCM to study feedbacks and hemispheric asymmetries related to the formation and recession of the seasonal carbon dioxide frosts, complex processes that are significantly affected by the meridional transport of atmospheric heat. The water cycle of the

NPRC is affected by midsummer polar weather; this has been examined through the use of 2-D models [*Jakosky*, 1983; *Haberle and Jakosky*, 1990] and 3-D models [*Houben et al.*, 1997; *Richardson and Wilson*, 2002; *Montmessin et al.*, 2004; *Bottger et al.*, 2005]. These studies collectively demonstrate a need to better understand the sources of water in the annual water cycle, as measured by the Mars Atmospheric Water Detector (MAWD) on Viking and the Thermal Emission Spectrometer (TES) on Mars Global Surveyor (MGS). *Haberle and Jakosky* [1990] suggested that the equatorward transport of water is severely limited by the weakness of the summertime circulation, which implies that 2-D dynamics cannot simulate the transport of water vapor, or that sources of water besides the NPRC are important in the observed annual water cycle. If the actual summertime atmospheric dynamics are too weak to sufficiently transport water vapor equatorward then the regolith may be an important source/sink in the annual water cycle [*Jakosky*, 1983; *Houben et al.*, 1997; *Bottger et al.*, 2005]. *Houben et al.* [1997] attempted to determine the capacity of the regolith by tuning this in their 3-D climate model to achieve the best fit to the observed water cycle; however, errors in their code (affecting the conservation of water mass) caused their results to be ambiguous (H. Houben, personal communication, 2004). *Richardson and Wilson* [2002] simulated the annual water cycle in a GCM without the need for an active regolith, although their columnar water mass abundances were too large by a factor of two, a problem that was also encountered by *Bottger et al.* [2005] when not using an active regolith. *Montmessin et al.* [2004] were successful in simulating the annual water cycle without using an active regolith; they suggest that their cloud scheme (which predicts cloud particle size) is key to this result, although they acknowledge that none of the GCMs are yet sophisticated enough to provide a definitive answer about the importance of the regolith versus the north residual cap in the annual water cycle. Mesoscale models may prove to be extremely useful in helping to quantify the importance of water from the NPRC in the annual water cycle due to their ability to full resolve the dynamics of the polar atmosphere.

[5] Given the relatively coarse grids that have been used in Mars grid point GCMs (and the low spectral truncations of spectral GCMs) these models cannot be expected to provide realistic representations of the smaller-scale circulations that will be important over the NPRC. GCMs traditionally rely on eddy diffusion to represent the effects of subgrid-scale circulations; in the vicinity of the NPRC these subgrid scales should be very important dynamically. Transient eddies in the summertime polar region almost certainly possess spatial and temporal scales that cannot be realistically represented with an eddy diffusion approach. Additionally, due to the convergence of meridians at the pole, the deformation of the grid box in grid point GCMs at high latitudes becomes highly problematic, even though latitude and longitude spacing is uniform; this is the "pole problem" of standard grid point GCMs. It cannot be the case that atmospheric variables should be assumed constant over much larger meridional than zonal spatial scales; there will in fact be very strong meridional gradients in polar circulations at latitudes where this problem is most pronounced in GCMs. Grid point GCMs typically use spatial filtering of some sort to minimize this "pole problem," making the zonal and meridional scales more similar. However, this approach is not as desirable as using unfiltered dynamics on computational grids that are most appropriate for polar studies. A Mars GCM that used an alternative computational domain (preserving the equivalence of horizontal scales near the poles) could be a very important new tool. As *Richardson and Wilson* [2002] point out, mesoscale models should be used to better understand the role of atmospheric dynamics in the polar region. By performing polar mesoscale studies at high-resolution, an improved description of atmospheric dynamics at high latitudes can be provided; this should help in quantifying the role of the NPRC in supplying water to the global water cycle.

[6] The smaller-scale dynamics of the polar atmosphere is a large uncertainty in modeling the annual water cycle; this is the first comprehensive high-resolution mesoscale model study of atmospheric dynamics at high latitudes. With polar stereographic domains, mesoscale models do not have a "pole problem." Moreover, mesoscale models allow for higher spatial resolutions, even beyond the limitations of the hydrostatic assumption (when studies at very high resolution are needed). In this study, moderate- to high-resolution simulations are used to examine summertime transient eddies, for which a broad size spectrum is expected, as indicated by imagery of summertime clouds [*Wang and Ingersoll*, 2002]. With high spatial resolution, mesoscale simulations must be shorter in duration because of greater computational requirements, a problem that is much exacerbated when using nonhydrostatic dynamics. This trade-off is the primary reason we have chosen to use hydrostatic dynamics in this study. At spatial scales only somewhat smaller than those examined here ($\sim$5 km) it is anticipated that nonhydrostatic dynamics should become important when simulating the stronger transient eddies found in the simulations described below.

[7] In this study we examine only a short period of the Martian year. This short period, from L_s = 120 to L_s = 150, is critical in the water cycle of the NPRC; it is constantly exposed to insolation and the maximum amount of water vapor in the polar atmosphere is seen during this season [*Smith*, 2004]. Moreover, during this seasonal period water ice clouds are relatively infrequent [*Smith*, 2004]; thus clouds can be neglected for a study that focuses on developing a better understanding of atmospheric dynamics at higher resolution. Finally, this season has a relatively complete observational record of surface temperatures and thermal properties (surface albedo and thermal inertia) with which to constrain the model and results. The NPRC is a physical record of the past that will ultimately yield a vast amount of information about climate history on Mars. Processes in the atmosphere are fundamental in the formation and evolution of the NPRC and the polar layered deposits [*Herkenhoff and Plaut*, 2000]. This dynamical study is a first step toward simulations of greater sophistication,

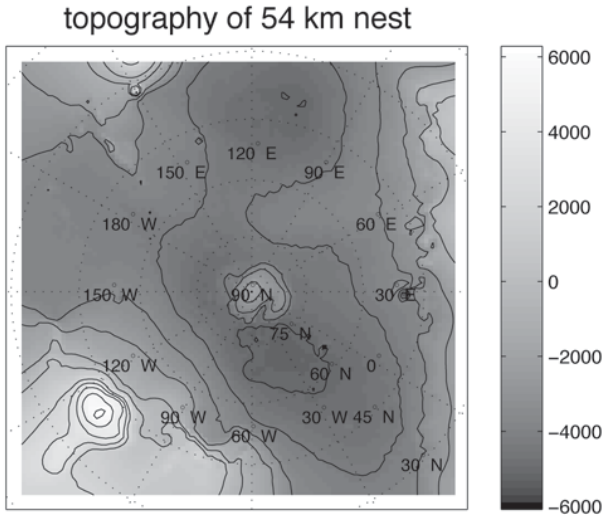

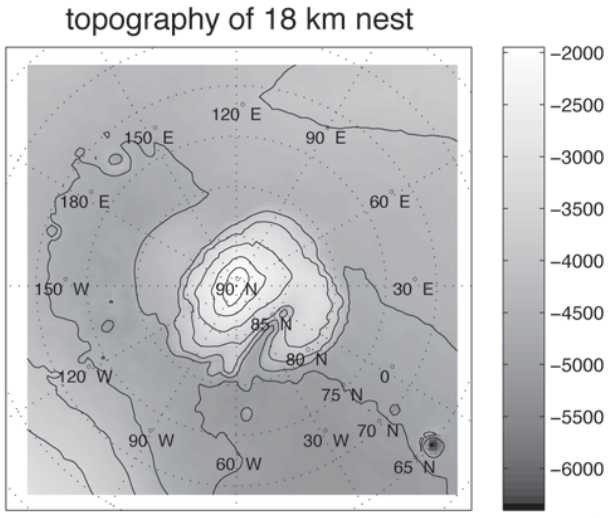

Figure 1. Topography of the two nests used in these simulations. Both nests are dynamically two-way during model integration. The 54 km nest is 100 × 100, whereas the 18 km nest is 109 × 109 grid points.

studies that will include water vapor transport and surface source/sink processes.

2. OSU MMM5 Specifications and Modifications

2.1. Model Description

[8] The mesoscale computer model used in this study is the Oregon State University Mars MM5 (OSU MMM5). *Tyler et al.* [2002] describe development and validation of the OSU MMM5 against Pathfinder and Viking lander observations. In short, the Penn-State/NCAR MM5 [*Grell et al.*, 1994] was modified to simulate mesoscale circulations in the atmosphere of Mars. The NASA Ames Mars GCM [*Haberle et al.*, 1999] provides initial and hourly boundary conditions for all OSU MMM5 simulations. The atmospheric radiation package used in the OSU MMM5 was taken from the Ames GCM. In this radiation package dust is "too dark" at visible wavelengths, due to an underestimation of the single scattering albedo (R. M. Haberle, personal communication, 2004). For this reason the visible dust opacity that is used to tune the OSU MMM5 to summer atmospheric temperatures (0.075) is somewhat low in comparison with TES observations of average global dust opacity during the seasonal period of this study.

[9] The OSU MMM5 has 32 sigma levels; the model top is at 0.03 mbar (∼40 km) and the lowest level is ∼1.7 m above the surface. Approximately 2/3 of these model levels are in the lowest atmospheric pressure scale height (∼10 km), providing very good vertical resolution near the surface of the planet. The hydrostatic version of the OSU MMM5 is used in this study; it uses a surface following sigma vertical coordinate that is identical in form to that of the NASA Ames Mars GCM:

$$\sigma = (p - p_{top})/(p_{sfc} - p_{top}). \quad (1)$$

Surface property maps of topography (MGS/MOLA), albedo [*Christensen et al.*, 2001] and thermal inertia [*Putzig et al.*, 2005] have been developed from high-resolution global maps for use in our modeling studies. Minimally smoothed versions of these global maps are used to construct maps at appropriate resolutions for use in both the Ames GCM and the OSU MMM5, maintaining consistency in all surface properties between the two models at the boundary of the mesoscale model (mother domain boundary).

[10] Because of differences between computational grids, model dynamics and the physical parameterizations used in GCMs and mesoscale models, reflections from model boundaries are to be expected in mesoscale models. These reflections can be problematic depending upon the choice of domains and the modeling objectives. With the large thermal tides in the Martian atmosphere this can become a significant problem. Using the same approach as *Tyler et al.* [2002] to minimize the effect of boundary reflections, the mother domain used in all of these simulations is semiglobal and polar stereographic. In these studies it has a nominal grid spacing of 162 km, covering the northern hemisphere and reaching to ∼30°S. Two sols after the simulations begin we initialize two higher-resolution nests; the first has a grid spacing of 54 km and the second (nested in the first) has a grid spacing of 18 km. The 18 km nest provides very good resolution of mesoscale circulations poleward of ∼65°N; both nests use "two-way" dynamics (they are thus affecting and affected by the next lower resolution nest). All three domains are centered on the North Pole of Mars; Figure 1 shows the topography of the two nests.

[11] Three simulations were performed for this study, at L_s = 120, L_s = 135 and L_s = 150, each for a total duration of 29 sols. The final 20 sols of each simulation are centered on the specific L_s of the run (solar forcing change with date during each run, consistent with the 29 sols of hourly GCM boundary conditions). For numerous reasons three separate simulations proved to be an easier approach than one long simulation; some of the reasons are related to the actual computer codes of the Ames GCM and the OSU MMM5 and others are simple consequences of the computational resources at our disposal for this study. These simulations

all use hydrostatic dynamics and the atmosphere is dry. At the resolutions used the assumption of hydrostatic dynamics should be valid. Hydrostatic dynamics significantly lessen the computational burden in comparison to the use of a nonhydrostatic dynamical core; this allows for longer simulations (good model statistics), an ability to "tune" the model to observations and to explore the sensitivity of results to changes in modeling domains and various modeling parameters.

[12] *Dudhia* [1993] developed the nonhydrostatic version of the MM5 on the basis of the work of *Klemp and Wilhelmson* [1978], who realized that certain terms in the pressure tendency equation, those which represent the contribution of diabatic heating and the convergence of subgrid-scale heat flux, can be neglected to save some computations (under terrestrial conditions the amplitude of these neglected terms is small compared with other terms in the equation). However, in a nonhydrostatic mesoscale model used to study Martian circulations these terms should probably not be neglected; diabatic heating in the atmosphere of Mars is very large and responsible for dramatic atmospheric thermal tides [*Wilson and Hamilton*, 1996; *Zurek and Haberle*, 1988]. As part of an international workshop to compare Mars mesoscale models it was found that the standard nonhydrostatic dynamical cores tended to cause an overestimation of the diurnal surface pressure cycle [*Tyler et al.*, 2003]. After the workshop, discussion between participants revealed that this problem is apparently a consequence of these terms being universally neglected in nonhydrostatic dynamical cores. The nonhydrostatic dynamical core of the OSU MM5 will soon be modified to include these neglected terms so either dynamical core can be used reliably in future studies; the MRAMS model (nonhydrostatic only) has already been modified accordingly (S. C. R. Rafkin, personal communication, 2004).

[13] At seasonal dates somewhat before or after this study, TES observations of NPRC surface temperatures can be significantly lower than those during the L_s = 120 to L_s = 150 period, indicating that carbon dioxide frost can still be found on the surface in early summer and can appear there significantly before fall equinox (L_s = 180). Thus simulating dates that are somewhat before or after this study period is somewhat inconsistent with the albedo and thermal inertia maps being used in the model (these maps are described below). To simulate conditions at earlier seasonal dates a retreating seasonal cap (visible and thermal edges) can be parameterized in the albedo and thermal inertia of the OSU MM5 based on observations; this approach yields a realistic thermal environment and is allowing simulations to be performed that are relevant to the EDL phase of the Mars Scout Phoenix mission ($L_s \sim 80$). For dates after this study period, into the fall and winter seasons, the model will require additional physics to simulate clouds and represent the condensation of carbon dioxide in the atmosphere and on the surface. Collaborations with members from the NASA Ames Mars GCM group will provide cloud schemes that can be included in the OSU MM5 so that fall/winter simulations can be performed in the future.

[14] Finally, since the sun remains at low angles above the horizon all day near the pole during this study period, and since topography can be fairly steep along the margin of the residual cap, it is important to include the effect that topographic slope will have on insolation incident on the surface. Recently the OSU MMM5 was modified so this important effect is included; we do not consider shadowing, since shadowing can largely be neglected at these spatial resolutions. For the 18 km nest, at the margin of the residual ice cap and for the walls of Chasma Boreale, we estimate that the effect of slope on the local noon and midnight surface insolation can be $\sim$10% over fairly extensive regions. A sensitivity simulation was performed for Valles Marineris when this functionality was first added to the model (not shown) that showed an enhancement of canyon wall slope flows (upslope and downslope) as large as $\sim$10 m/s. The enhancement of winds in these simulations will be much smaller in response to the topography of the NPRC.

2.2. Thermal Inertia Map Construction

[15] The near-surface thermal environment is critical to the development of mesoscale circulations on Mars. To realistically simulate high-resolution dynamics near the NPRC it is very important that the thermal environment is well represented; thus the surface thermal properties (albedo and thermal inertia) must be specified as accurately as possible. Data collected by the MGS TES have yielded a high-quality global map of surface albedo [*Christensen et al.*, 2001] and these data are used in the OSU MMM5.

[16] Thermal inertia (the square root of the product of thermal conductivity, density and heat capacity: $I \equiv (k\rho C)^{1/2}$) is not an observable quantity; it is determined through modeling and the quality of the result depends upon sufficient availability of accurately measured nighttime surface temperatures; these measurements become sparse to nonexistent for the highest latitudes in the TES data set (a consequence of the 0200 and 1400 local time mapping orbit). Derived thermal inertias are influenced by the amount of subsurface ice, which can cause the apparent thermal inertia to vary significantly with season; this is a problem that is more pronounced at high latitudes where subsurface ice is most prevalent. Moreover, atmospheric processes and clouds can significantly influence the evolution of nighttime surface temperatures; these effects are difficult to represent accurately in the process of modeling thermal inertia. At present, *Putzig et al.* [2005] are providing the best thermal inertia maps and they are also actively refining their modeling methods; the data they have made available to the community is complete from 80°S to 80°N, which does provide thermal inertia data on the NPRC for some longitudes. Using reasonable extrapolations, this high-latitude coverage allows the construction of a thermal inertia map that is complete in the polar region.

[17] We apply three simplifying assumptions to replace the missing thermal inertia data over the polar region: (1) the thermal inertia of the brightest albedo ice surfaces is well represented with a single value (800 J m^{-2} K^{-1} $s^{-1/2}$, the maximum value shown in the *Putzig et al.* [2005] map); (2) the nature of the thermal inertia gradient observed at the margin of the residual ice cap at certain longitudes is representative for the margin of the entire NPRC, producing a high correlation with surface albedo; and (3) a mean high-latitude thermal inertia value is appropriate for

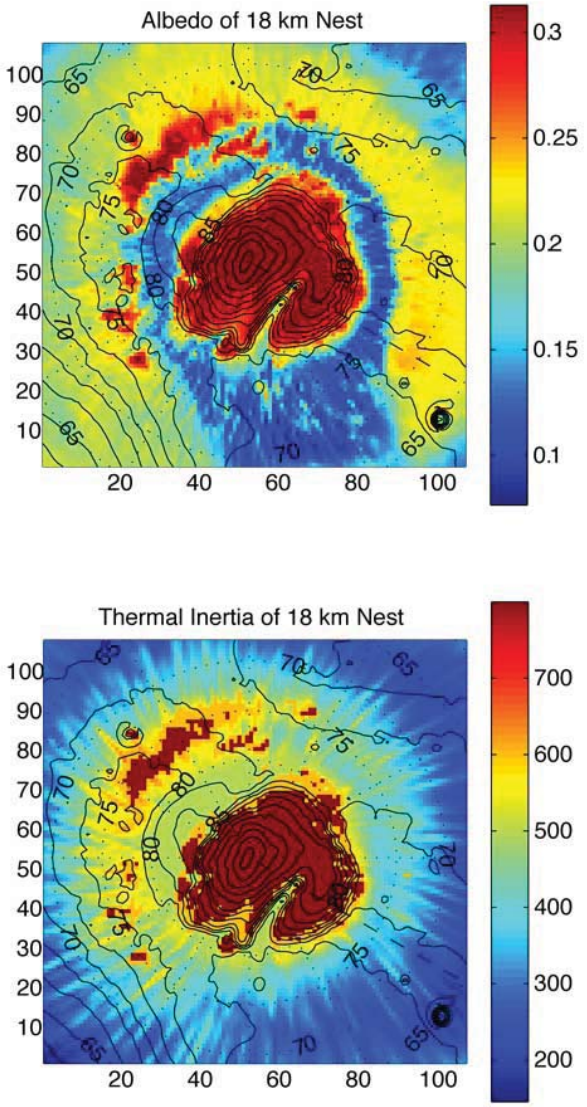

Figure 2. Albedo and thermal inertia from the 18 km nest are shown. The SI units of thermal inertia, as given in the color bar, are J m^{-2} K^{-1} $s^{-1/2}$. The zero meridian is shown with a black dashed line. The abscissa and ordinate count grid points in the domain; the 18 km nest is 109 × 109 grid points.

lower-albedo locations that are missing data above 80°N (500 J m^{-2} K^{-1} $s^{-1/2}$). Using these assumptions our thermal inertia map is completed to the pole and the transition at 80°N is smooth. This high-resolution map was used to construct all of the maps, at appropriate resolution, that are used in both models for these simulations. The albedo and thermal inertia data for the 18 km nest are shown in Figure 2. Correlation between thermal inertia and the brightest albedo data is apparent, including the outlier ice deposits; this is logical if one assumes that the brightest albedo regions are also high thermal inertia ices that reach a significant depth into the subsurface. Our thermal inertia map does show a greater correlation with albedo than that of *Paige et al.* [1994], although the overall structure is quite similar. Specific regions such as the inner reaches of Chasma Boreale and Olympia Planitia have been assigned the assumed data-fill value (500 J m^{-2} K^{-1} $s^{-1/2}$). Comparing modeled surface temperatures and those observed by TES suggests this value works fairly well (see below). Tuning this parameterization, so that modeled results better matched surface temperature observations, involved adjusting the transition values for the assumptions used to produce the thermal inertia values as described above.

2.3. Comparing Modeled Temperatures With Observations

[18] In addition to constructing thermal inertia maps we needed to modify the method used for initializing temperatures at the base of the soil model in the OSU MMM5; this is key to achieving realistic NPRC surface temperatures in the model. At locations assumed to be predominantly nonice to a depth greater than the soil model (0.5 m), temperatures at the base (constant-valued throughout the simulation for each location) are determined by spatial interpolation of the diurnal mean GCM surface temperature (this is the normal MM5 approach). However, since the residual ice cap is poorly resolved in the Ames GCM (resolution of 7.5° in latitude), this method cannot provide a realistic temperature structure for the base of the soil model below the NPRC in the higher-resolution nests. Clearly, the stratigraphy of the subsurface is unknown, although it seems reasonable to assume that the fractional amount of ice in the top 0.5 m correlates fairly well with surface albedo, especially for the brightest locations. Moreover, in describing the summertime energy budget of the NPRC, *Paige and Ingersoll* [1985] showed that a substantial heat flux into the subsurface is needed. Their finding provides the fundamental rationale for modifying our soil model initialization in the OSU MMM5 in the following way: for high-albedo locations ("ice" surfaces) we initialize the deep soil temperature at 175 K, which is an average between the ~200 K summer and ~150 K winter surface temperatures. With this modification and our thermal inertia maps the simulated surface temperatures and the magnitude of the diurnal surface temperature cycle agree well with the TES observations for high-latitude locations.

[19] We compare the TES surface temperatures with the 20-sol mean maximum and minimum model surface temperatures in Figure 3; the OSU MMM5 data were taken from the L_s = 135 18 km nest. The maximum temperatures in the model occur close to 1400 Local Solar Time (LST), whereas the minimum temperatures occur close to 0300 LST. Because of the MGS mapping orbit, the actual LST of these TES observations varies significantly at high latitudes (from 70°N to 85°N the "2 pm" LST decreases with latitude from 1400 to 1200, while from 70°N to 82.5°N the "2 am" LST increases with latitude from 0300 to 0400). The daytime maximum temperature comparison is actually very good, especially since the largest differences in LST occur on the residual cap where the amplitude of the diurnal surface temperature cycle is small. The model is slightly cool in Olympia Planitia and slightly warm equatorward of the circumpolar dune

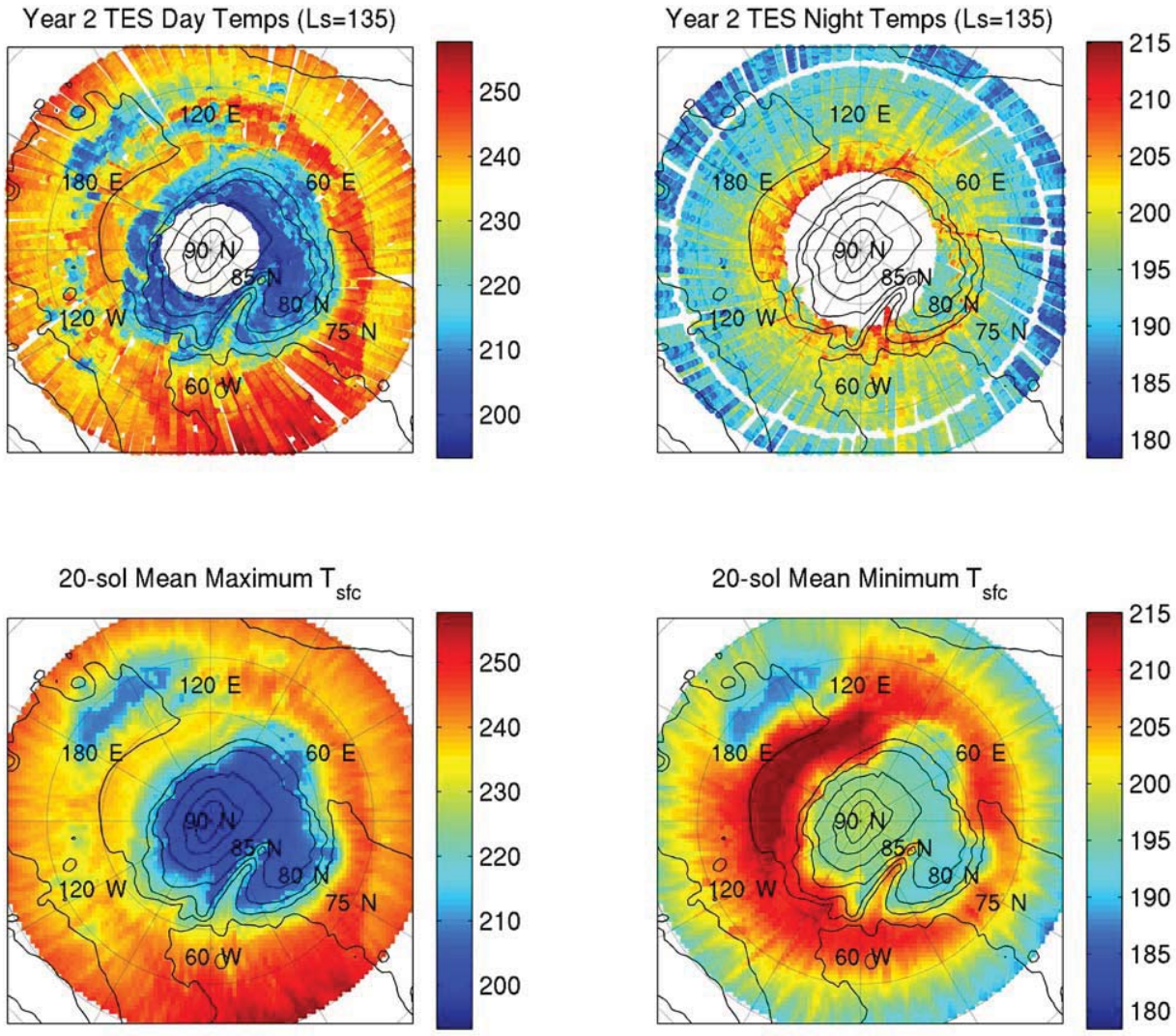

Figure 3. A temperature comparison between TES surface temperatures (0200 and 1400 LST) and 20-sol mean maximum and minimum temperatures in the 18 km nest of the L_s = 135 simulation. The solid black lines are uneven intervals of topography; the 18 km nest temperatures were cropped to facilitate comparison with observations at 70°N.

fields (75°N, 60°E), although there does not appear to be any systematic bias in the comparison of the maximum surface temperatures. However, the nighttime minimum temperature comparison shows a noticeable warm bias in the model; the model is consistently ~5 K too warm away from the NPRC or the outlier ices (77°N, 160°E). For the warmest region in the model minimum temperature map (Olympia Planitia), our mean high-latitude thermal inertia (500 J m^{-2} K^{-1} $s^{-1/2}$) is probably too large [*Paige et al.*, 1994], especially since this location appears slightly cool in the maximum temperature comparison. With the exception of the outlier ices, for latitudes equatorward of 80°N the *Putzig et al.* [2005] thermal inertia data was used without modification. Their thermal inertia values appear to be somewhat large at these latitudes for this season. Subsurface ice is presumably playing a role in affecting surface temperatures and some modeling efforts have found favorable results after modifying their treatment of the subsurface to more realistically account for ice (R. J. Wilson, personal communication, 2005). Such modifications might be very important in terms of correctly simulating the water cycle of the NPRC and the surrounding region since small errors in air temperature near the surface can produce dramatic variation in the amount of water that the atmosphere will hold at saturation. However, in terms of simulating summertime circulations at higher spatial resolutions (the primary focus of this study) these relatively small temperature disagreements should not have much effect.

[20] In the context of atmospheric temperatures, both the Ames GCM and the OSU MMM5 assume a globally uniform atmospheric dust distribution. In all three simulations we use a total visible optical depth of τ = 0.075. A somewhat larger value ($\tau \sim 0.1$) would be in better

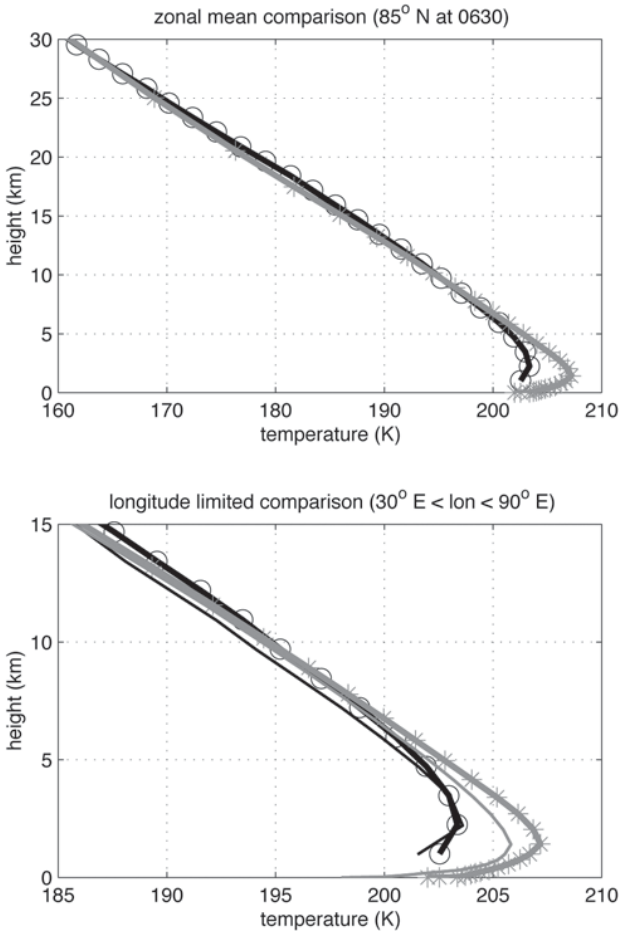

Figure 4. The top subplot is a comparison between the zonal-mean OSU MMM5 temperature profile and a zonal mean constructed from RS data at 85°N. The RS profile (heavy black line, circles) is for a seasonal date of L_s = 135, an LST of 0630, and a mean latitude of 85°N. The OSU MMM5 zonal-mean profile was constructed from the 18 km L_s = 135 output at 85°N and 0630 LST (heavy gray line, asterisks). In the bottom subplot the additional thin black and gray lines show temperature profiles created using a limited range of longitude (30°E < longitude < 90°E), for profile locations that are far from the cap edge.

quantitative agreement with actual TES observations, although the overly dark GCM dust requires a lower opacity to match the thermal data; however, the assumption that the total optical depth is globally uniform is not a bad one for most of this study period [*Smith*, 2004]. With the atmospheric radiation code used in our version of the Ames GCM, as well as the OSU MMM5, τ = 0.075 yields an agreement with MGS/TES atmospheric temperature observations (not shown) that is felt to be adequate for this study. By L_s = 150, the assumption that dust is distributed uniformly over the globe becomes less valid, although this study reaches conclusions about the nature of the circulation at this date that would only be enhanced if a more realistic treatment of atmospheric dust was used in our modeling. Additionally, τ = 0.075 provides good agreement with high-latitude (85°N) Radio Science (RS) temperature profiles [*Hinson et al.*, 2001] in the polar region where we have purposefully taken the greatest care to accurately represent the thermal environment.

[21] In tuning the model to agree with high-latitude temperature observations we used a large number of RS temperature profiles (evenly distributed in longitude) to construct a zonal-mean RS temperature profile. The individual RS temperature profiles are evenly and tightly centered on L_s = 135, a LST of 0630 and a latitude of 85°N. The resulting RS zonal-mean temperature profile is compared with an OSU MMM5 zonal-mean profile in the top subplot of Figure 4. The OSU MMM5 profile was constructed using output from the 18 km nest at L_s = 135, interpolated to 0630 LST and 85°N.

[22] Comparing temperatures over the NPRC at 85°N was useful in checking our thermal inertia map. The latitude circle at 85°N is often perpendicular to the sharpest gradients in surface albedo and is thus located where transitions occur in our thermal inertia prescription (thermal inertia, driven by the amount of ice in the "soil," correlates with albedo), as seen in Figure 2. The simulated zonal-mean temperature profile agrees very well with the zonal-mean RS profile at altitude, primarily a consequence of the dust opacity. However, in the lowest ~5 km the OSU MMM5 exhibits a stronger inversion than seen in the RS temperature profile; this is somewhat due to the proximity of individual temperature profiles in the modeled zonal mean to the thermal edge of the NPRC (discussed below). Our final thermal inertia prescription was settled upon by adopting the following basic premise: as albedo drops rapidly from the brightest locations, the subsurface is still mostly ice and subsurface heat flux remains important in the surface energy budget. The extent to which the subsurface remains ice equatorward of the brightest NPRC albedo values may be very important in terms of local circulations. Recent measurements of water ice in the Martian polar subsurface [*Boynton et al.*, 2004; *Prettyman et al.*, 2004] suggest that there is a significant amount of ice in the subsurface away from the residual cap; our approach may underestimate this somewhat, as also suggested above in discussing the minimum surface temperatures in the polar region.

[23] Even though the OSU MMM5 results agree quite well with the observed diurnal amplitude of surface temperature on the NPRC, it can be noted that the inversion in the simulated temperature profile of Figure 4 is stronger than in the RS data. This could be due to one or more of the following: (1) the PBL scheme in the OSU MMM5 (which uses terrestrial parameters and scaling) may be causing the near-surface temperature structure to be somewhat unrealistic; (2) the RS and modeled temperature profiles differ too much in footprint, which causes the comparison near the surface to be less valid than it is at altitude; (3) the RS temperature profiles underestimate the strength of the inversions; or (4) water ice clouds are present over the NPRC and affect the atmospheric temperatures at low levels. We believe that the RS temperature profiles underestimate the near-surface inversions to some degree; sharp changes in the vertical gradient of temperature would certainly be somewhat smoothed out in the retrieval process (D. P. Hinson, personal communication, 2003). Additionally, there may be

a bias in the retrieved temperatures very near the surface due to water vapor [*Hinson et al.*, 2004]. Ice cloud effects are a possible factor, although an examination of these is beyond the scope of this study.

[24] Since the thermal NPRC in the OSU MMM5 is a little small, as evidenced by the temperature comparisons of Figure 3, the near-surface temperatures in the OSU MMM5 at 85°N may be somewhat warmer than they should actually be (some of the profiles used to construct the zonal mean are nearer the thermal edge of the cap than in reality). To examine this possibility we created a longitude-limited temperature profile comparison from a region of the cap where all profiles are far from the edge of the NPRC; this is shown in the bottom subplot of Figure 4. The heavier lines are the zonal-mean profiles as in the top subplot; the thin lines are the longitude-limited profiles. Since the agreement is indeed better between the longitude-limited profiles, we suspect that cap edge effects are causing some of the disagreement between the zonal-mean profiles.

3. Results

[25] The nesting capability available in mesoscale models allows for the examination of model output at multiple scales within a single simulation. Mother domain results should demonstrate consistency with larger-scale GCM simulations and can additionally be used to compare against spacecraft observations of atmospheric temperatures, such as those from TES. Results from the higher-resolution nests will then be useful in revealing smaller-scale circulations and their influence on the larger-scale atmospheric structure and the climate of specific regions.

[26] As described above, GCMs are not optimal tools for simulating atmospheric dynamics in the polar region because of low spatial resolutions and the "pole problem." With the domains being used in these mesoscale simulations such problems are avoided; however, to more realistically simulate polar dynamics, and assure that the model is capturing the larger-scale circulation, a basic trade-off is accepted. A mother domain of significant size (100×100 in these simulations) is needed to avoid reflections from mesoscale model boundaries. With the polar stereographic projection being used here the true model resolution is somewhat less than nominal near the pole (where greater resolution is most desired), although greater than nominal at the mother domain boundaries (where it is not needed). The nests that are being used in this study add significant computational overhead, but provide the higher resolutions that are needed in this study.

[27] The central focus of this work is to provide a high-resolution characterization of the polar atmospheric circulation, specifically a characterization of the transient eddy activity during northern summer. Transient eddies can form in many ways, and the processes that cause their formation occur over a wide range of spatial scales. The large-scale circulations and their zonal asymmetries, and well-resolved regional and smaller-scale circulations, drive a surprisingly vigorous and complex summertime polar circulation. To begin characterizing the midsummer circulations in the OSU MMM5 we first examine the zonal-mean fields of the mother domain in comparison with those from the Ames GCM.

3.1. Zonal-Mean Fields

3.1.1. Large-Scale Zonal Means and Zonal Asymmetry

[28] The OSU MMM5 has a much lower model top in comparison with current Mars GCMs, 3×10^{-2} mbar (~40 km) versus 5×10^{-5} mbar (~90 km) for the Ames GCM that is being used in this study. Since the mother domain boundaries are interacting with GCM boundary conditions in the southern hemisphere, it is useful to verify that the mother domain circulations reproduce the characteristic features of the northern summer general circulation as predicted by the Ames GCM. A basic comparison can be made between zonal-mean meteorological fields from the OSU MMM5 and those from the Ames GCM, specifically the zonal-mean fields of zonal velocity, meridional velocity and atmospheric temperature (U, V and T).

[29] There are two approaches when constructing zonal-mean fields from a sigma vertical coordinate model: (1) construct zonal means on sigma levels and then transform to a pressure vertical coordinate or (2) first interpolate output onto pressure surfaces and then construct the zonal means. The first approach produces results right down to the surface and is thus needed for determining the zonal-mean flow very near the surface. The second approach is better for an examination of circulations higher in the atmosphere and more useful in some analyses. We use the first method here, since we are primarily interested in mesoscale circulations in the lower atmosphere. Mother domain zonal-mean fields are shown for all simulations in Figure 5a; these data were constructed from twenty sols of hourly data that is centered on the specific L_s of each simulation. In Figure 5b the zonal-mean fields from the Ames GCM are shown for the same period.

[30] Between $L_s = 120$ and $L_s = 150$, as the subsolar latitude moves south from ~22°N to ~12°N, the zonal-mean temperature structure responds accordingly in both models. Poleward of ~80°N temperatures in the lower atmosphere of the OSU MMM5 decrease significantly (~20 K) over this period. Similar changes also occur in the Ames GCM, although the gradients and amplitudes are larger in the OSU MMM5 because the NPRC is more realistically represented. The zonal-mean zonal wind fields in Figure 5a show the lower reaches of the lower-latitude easterly jet, much as seen for the GCM in Figure 5b. As expected, this jet weakens with L_s over the period of this study in both the GCM and the mesoscale model. As in the GCM, the mesoscale model has weak equatorial easterlies near the surface and exhibits similar changes in their structure over the period of this study. By $L_s = 150$, in response to a rapidly cooling polar environment and a growing meridional temperature gradient, an early fall polar jet has begun to form in both models. This jet marks the onset of strong transient circulations that are much like winter baroclinic storms (discussed later). The zonal-mean meridional winds are much weaker (note color bar) and change less during the period of this study than do the zonal-mean zonal winds. The most obvious change is in the poleward flow near the surface, which is seen in Figure 5a and Figure 5b. The southward flow in the top left of each

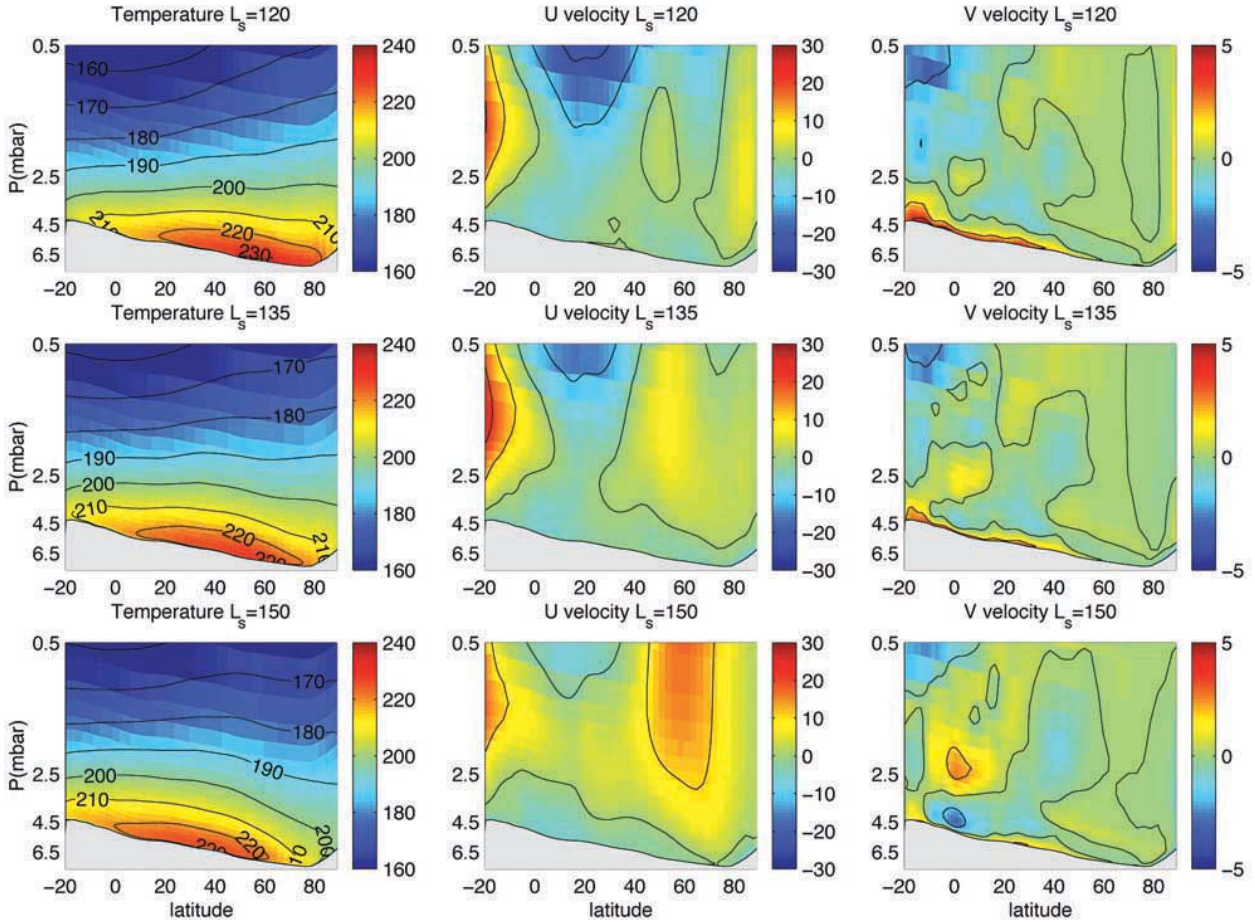

Figure 5a. Zonal-mean fields from the mother domain are shown for each simulation (complete longitudinal coverage exists in the mother domain to 20°S). The zonal-mean averages were generated on sigma surfaces and then a coordinate transformation was performed onto corresponding zonal-mean pressure levels. Each of the subplots shows a 20-sol zonal mean that is centered seasonally on the L_s of the simulation.

meridional wind subplot is part of the upper branch of the Hadley Cell; as expected, this flow weakens with time in both models. Such basic agreements between the zonal-mean fields of the two models show that the OSU MMM5 is satisfactorily reproducing the large-scale circulations as seen in the Ames GCM. However, even at the relatively coarse resolution of the mother domain there are some important differences.

[31] Because the NPRC is more realistically represented in the OSU MMM5, two flow features are seen in the zonal-mean winds of the mother domain that do not appear in the GCM zonal means: (1) a relatively weak westerly jet exists over the residual cap at L_s = 120 (~5 m/s), and (2) weak near-surface easterlies are seen over the residual cap in each simulation. These flows form in response to the thermal environment of the NPRC and are seen even more clearly at high resolution in the zonal-mean fields of the 18 km nest (next section). Such high-latitude features of the zonal-mean circulation, which are not typically well represented in GCMs due to low spatial resolutions and the "pole problem" (as discussed above), are quite important for the climate of the NPRC.

[32] All flow near the surface is explicitly included when constructing the zonal-mean fields of Figure 5a. Moreover, flow near the surface in the OSU MMM5 is well simulated due to the vertical resolution of the model in the lowest-pressure scale height. Because of topography and the large diurnal amplitude of surface temperature on Mars, slope flows can be "continental" in scale; these flows can modify the diurnal cycle of surface pressure when they converge into or diverge from basins [*Tyler et al.*, 2002]. For the zonal-mean meridional winds shown in Figure 5a, the largest changes in the flow are near the surface; it is useful to consider what processes produce this flow and why it changes during this short seasonal period.

[33] At L_s = 120 the strongest zonal-mean meridional winds near the surface extend significantly poleward of where they would be expected to terminate if this flow were simply the lower branch of the Hadley Cell; thus this feature is a consequence of more than one circulation and multiple mechanisms are required to explain it. It weakens between L_s = 120 and L_s = 135, but more so near the equator (south of ~10°N) than at higher latitudes. In the mesoscale model the northern part of this poleward flow persists even after

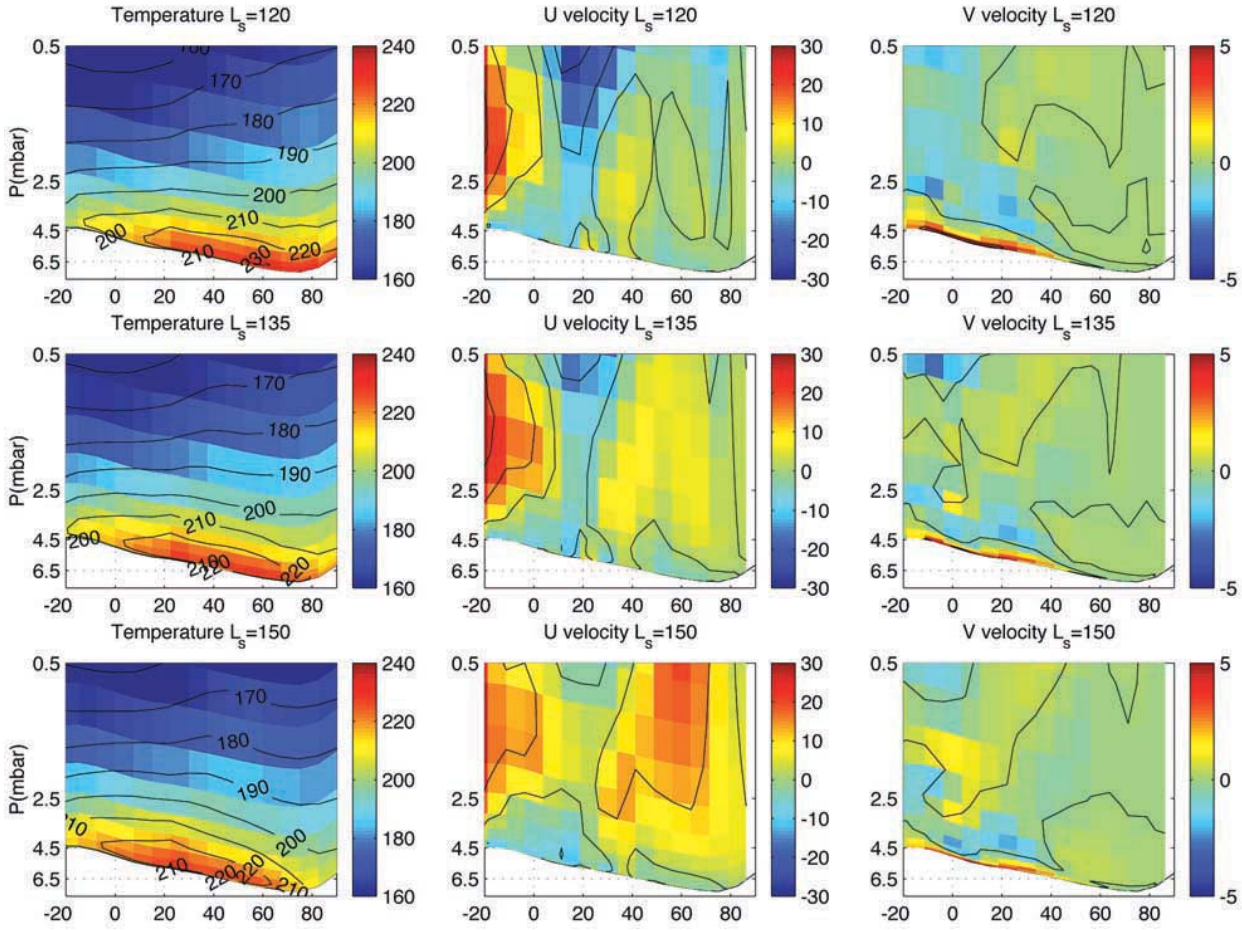

Figure 5b. Zonal-mean fields from the Ames GCM are shown for the identical period as shown for the mother domain in Figure 5a. The pressure, latitude, and color bar axes are the same as in Figure 5a.

the southern part has all but disappeared by L_s = 150; in the GCM the southerly portion of this flow maintains some strength at L_s = 150. The northern section of this flow is likely not a part of the Hadley Circulation, as the southern portion seems to be (it is reversing with the approach of fall equinox). We suggest that three different mechanisms contribute in causing the northern portion of this flow: thermal low-pressure circulations, slope flows and western boundary current effects. *Joshi et al.* [1995] describe western boundary currents in their GCM simulations; western boundary currents are a consequence of the Hadley Circulation being channeled along the western boundaries of huge topographical basins. Because of the dramatic topography of the volcanoes on Mars, large thermal low-pressure circulations will form over the volcanoes. With horizontal and vertical overlap, these two very different circulations can produce strong poleward flow at specific locations. The strongest winds associated with thermal low-pressure circulations form at altitudes above those of the strongest western boundary current effects; however, these two circulations will accelerate the same air where they overlap nearer to the surface. Slope flows will likely play an important role in the resulting diurnal mean winds. Slope flows on Mars are difficult to isolate since they exist over large regions and their effects are difficult to separate from other types of circulations (or even from other slope flows) within complex large-scale topography, such as that near Tharsis.

[34] To better visualize the interaction of these circulations we examine Figure 6, which shows the 20-sol diurnal mean wind field at sigma level 22 (~1 km above the surface). Wind vectors (length is proportional to speed) for each simulation are shown in subplots on the left and the color subplots on the right show wind speed. Over Elysium Mons, Olympus Mons, Alba Patera and each of the Tharsis Montes we find strong thermal low-pressure circulations. The strongest diurnal mean winds are generally related to these circulations. Over Elysium Mons and Alba Patera these flows are clearly cyclonic (counterclockwise). Over Elysium Mons we see that the northward flow on the east flank of the volcano is stronger, which may be evidence of a western boundary current enhancing the flow; this may also be evidenced by the gyre that develops in the region between Arcadia Planitia and Amazonis Planitia. Elysium Mons is quite isolated from the other volcanoes, explaining why the thermal low-pressure circulation over this volcano is more clearly defined.

[35] The flow over Alba Patera and Tharsis is a complex juxtaposition of many interacting circulations. Considering the complex flow around the volcanoes of Tharsis, we

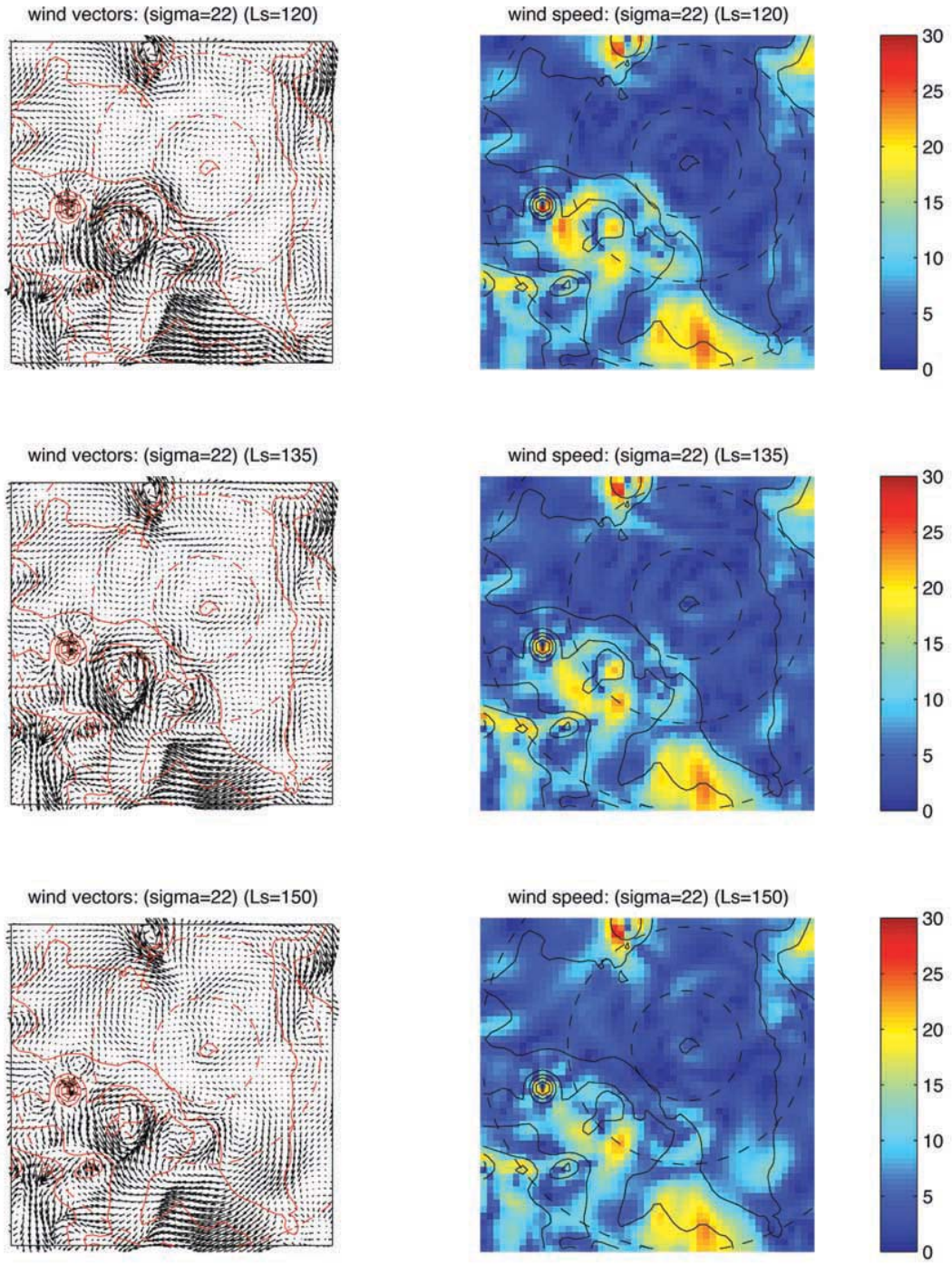

Figure 6. The diurnal mean wind field (a 20-sol mean) is shown for a subset of the mother domain at $\sigma = 22$ ($\sim$1 km). The left subplots show wind direction (arrow length is proportional to wind speed); the topography and latitude are contoured in red. The right subplots show wind speed in color with topography and latitude contoured in black (parallels at 30°N and 60°N and the equator are shown in each subplot).

develop a sense for the large scales over which slope flows and thermal circulations interact. For this reason the circulations over Tharsis and Alba Patera are far more complex than those over Elysium Mons. Within this complexity we suspect that the stronger northward flows on the northeast slopes of Tharsis, along the western boundary of Isidis Planitia and possibly on the eastern flanks of Elysium Mons are all at least somewhat influenced by western boundary currents. The thermal low-pressure circulation that exists over the huge topographical massif of Alba Patera and Tharsis is very strong; accelerations resulting from this circulation and a western boundary current effect would

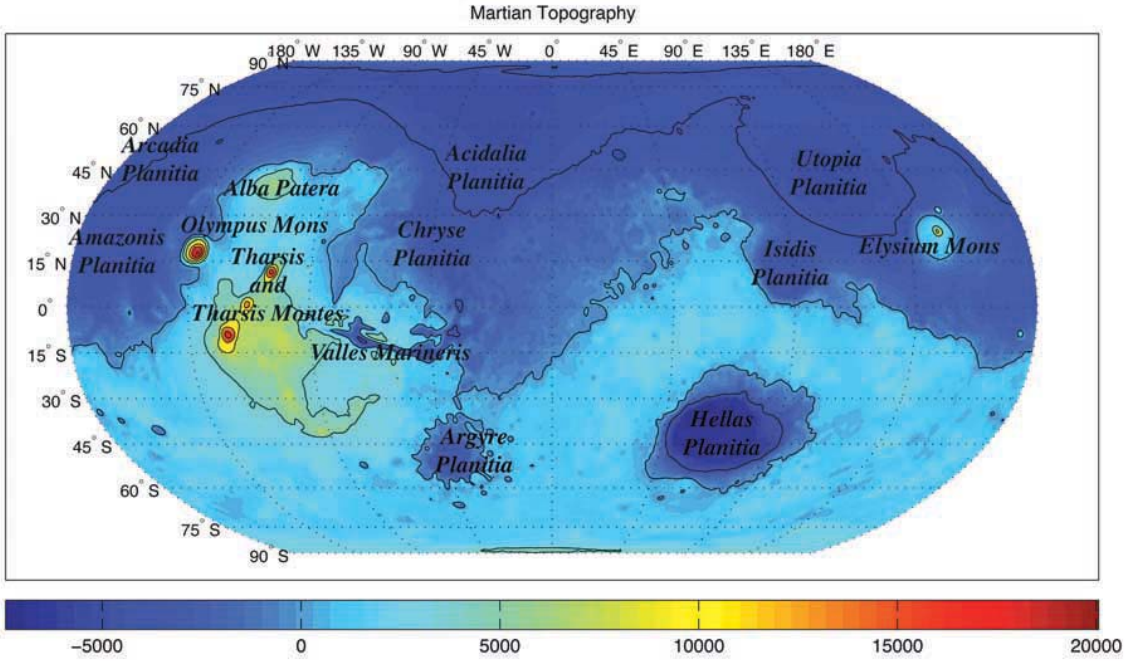

Figure 7. A global map of MOLA Martian topography is provided, with the geographical and topographical landmarks referred to in the text labeled for convenience.

be additive and produce a net northward flow, which may be important for the zonal-mean meridional flow feature seen near the surface at L_s = 120. On the east and west flanks of Alba Patera the respective northward and southward meridional flows do not change equally with time as if they were the meridional components of a single thermal circulation, although at greater altitudes they do (not shown). This suggests that the northward flow, which remains more constant with solar longitude, is influenced by another circulation, a western boundary current or the development of a stronger slope flow. The result of these changing circulations, and the overall weakening of the Hadley Circulation, produces the changes in the zonal-mean meridional flow near the surface. To aid in the identification of the topographical and geographical landmarks mentioned above we provide Figure 7, a global map of Martian topography with labels for each of these features.

3.1.2. High-Resolution Polar Zonal-Mean Fields

[36] In addition to comparing the zonal-mean fields of the mother domain with those from the GCM, it is instructive to examine the zonal-mean fields at much higher resolution over the most polar latitudes. Poleward of 70°N, the 20-sol zonal means of *U*, *V* and *T* from the 18 km nest are shown in Figure 8. As with the zonal-mean temperature in the mother domain, temperatures poleward of ~80°N are seen to decrease sharply (~20 K) between L_s = 120 and L_s = 150. Since the resolution of this nest is a factor of nine greater than the mother domain, the model dynamics can fully respond to the thermal forcing, providing a realistic representation of the zonal-mean circumpolar easterlies and off-cap katabatic winds. These flows are driven by a high-pressure center over the NPRC and the equatorward sloping topography of the cold residual cap (katabatic slope flows). Although these zonal-mean flows are somewhat weaker at L_s = 120, the circumpolar and katabatic winds are prominent features of the summertime circulation over the NPRC. The circumpolar easterlies scale with a depth of ~1.5 km, while the katabatic off-cap meridional winds are only ~1/5 as deep (~300 m). Near the surface the winds blow ~20° down-slope of the topographical contours at speeds between ~5 m/s and ~10 m/s. When overlaid on an image of the NPRC, the diurnal mean winds at the lowest model level (~1.7 m) are generally oriented roughly perpendicular to the NPRC spiral troughs (not shown). The spiral troughs are certainly suggestive of aeolian processes, and may have formed in response to winds [*Howard*, 2000]. However, if the ice of the NPRC undergoes glacial flow then the morphology of the spiral troughs may be far more complex [*Hvidberg*, 2003]. At L_s = 135 the zonal-mean winds are most representative of the actual near-surface wind regime over the NPRC. By L_s = 150 the polar environment is becoming significantly influenced by strong baroclinic storms that form in response to the development of an early fall polar jet. Throughout the entire study period there is a fairly strong overturning circulation at the edge of the NPRC; this overturning mean circulation is strongest at L_s = 135 when transient eddies are least prominent over the NPRC.

3.2. Transient Eddy Circulations

[37] Transient eddy circulations are very important in transporting heat and momentum into the northern polar region during winter. Northern winter storms are generally much stronger than those of southern winter, as has been shown by analysis of TES atmospheric temperature retrievals [*Banfield et al.*, 2004; *Barnes*, 2003a, 2003b]. Additionally, GCM studies show that the topography of the northern hemisphere plays an important role in producing stronger winter storms than those found in southern winter [*Barnes et al.*, 1993]. This work shows that topography is also

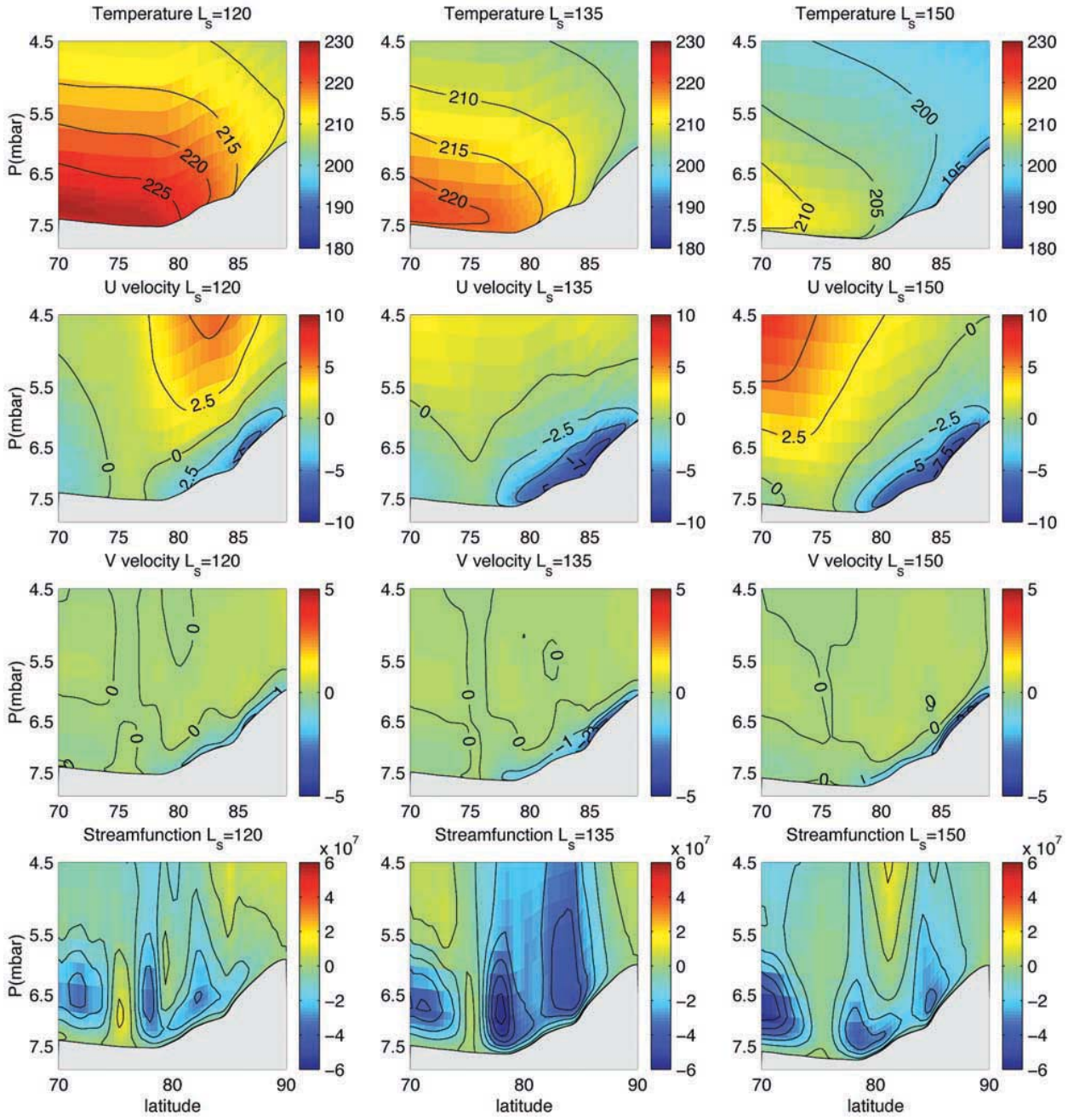

Figure 8. The 20-sol zonal-mean fields are shown for the 18 km nest for all three simulations: L_s = 120, L_s = 135, and L_s = 150. As an aid to understanding change in the meridional zonal-mean flow, the mass stream function is provided in the bottom subplots (stream function units are kg/s).

important in the formation of high-latitude transient circulations during summertime. Transient eddies in these simulations significantly influence the weather over the NPRC, and these circulations can even traverse large meridional distances to do so. Excited in part by the topography, these circulations form in preferred locations that change over the course of this study period in response to the changing large-scale circulation and thermal environment. Examining the poleward fluxes of heat and momentum from these transient circulations shows that they are climatologically very important during summer.

[38] We extract transient excursions from model output using a straightforward but robust method. From twenty sols of fully spun-up model output, we construct hourly mean cycles of U, V and T for all locations. With a second pass through the same model output, subtracting the local hourly means from the instantaneous values, 20-sol records of meteorological excursions from the mean diurnal cycles are constructed, as defined for zonal velocity by

$$u'(\lambda, \phi, z, t) \equiv u(\lambda, \phi, z, t) - \overline{u}(\lambda, \phi, z, hr). \quad (2)$$

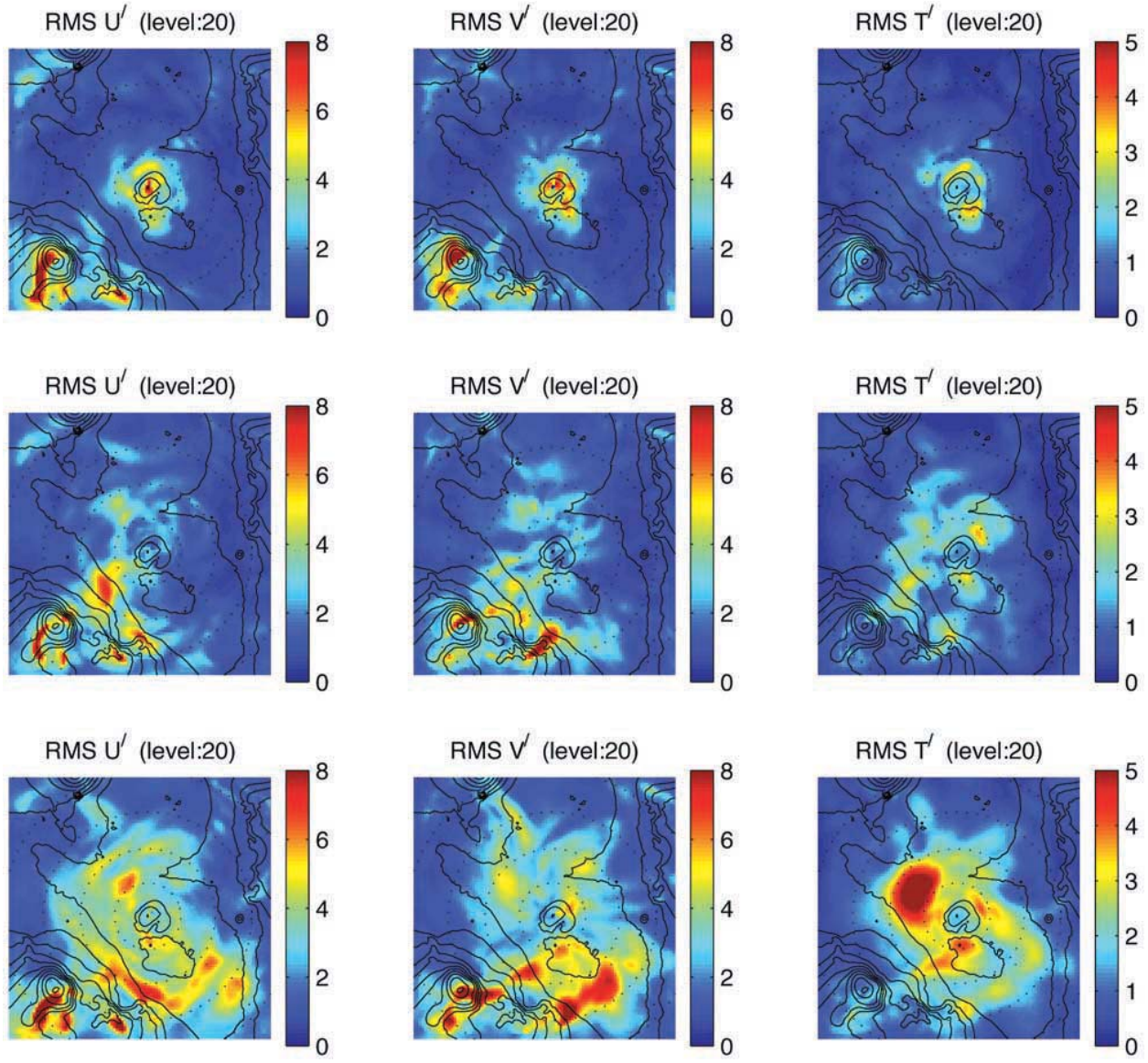

Figure 9. RMS values of meteorological excursions from the mean diurnal cycles of *U*, *V*, and *T* are shown at $\sigma = 20$ ($\sim$1.5 km) in the 54 km nest for each simulation: $L_s = 120$, $L_s = 135$, and $L_s = 150$.

[39] To produce the best records of transient excursions the model must be completely spun-up before the 20-sol period begins; to assure this we neglect the first nine sols of model output (seven for the nests that initialize two sols into the run). This may seem an excessive amount of spin-up time; however, considering that the model is initialized from coarse GCM output, the highly parameterized initial state of the NPRC and that larger-scale circulations develop in the OSU MMM5 (that are not well represented in the GCM initial conditions), it really is not. Experience with our model consistently indicates that significant spin-up times are important, especially for the polar region. The 54 km and 18 km nests are the most demanding, requiring all seven sols for the NPRC subsurface temperatures to equilibrate and for circulations to mature and adjust to the topography at high resolution. In this study we assume that twenty sols is a short enough period that change in the mean diurnal cycles (due to seasonal trends) is small, but long enough to characterize the mean state and to extract the transient circulations from each simulation. An examination of the hourly level-mean values of wind speeds and atmospheric temperatures, for all levels in both nests for the entire duration of these simulations (not shown) shows this is true and suggests that $\sim$2–3 cycles of natural variability are captured during a 20-sol period. At $L_s = 135$ the mean diurnal cycles do appear to be changing more rapidly than at $L_s = 120$ or at $L_s = 150$, showing $L_s \sim 135$ to be a period of transition for the climate of the polar region.

[40] In each simulation of this study we find that specific regions experience more inter-diurnal variability than others. These regions are seen in Figure 9, which shows the 20-sol RMS excursion amplitudes for the 54 km nest at sigma level 20 ($\sim$1.5 km altitude). RMS values are shown

in Figure 9 for the excursions of U, V and T, as defined for excursion zonal velocity by

$$\overline{u}'(\lambda,\phi,z) \equiv \text{SQRT}\sum_{t=1}^{t=N}\left[\left(\frac{1}{N}\right)\left(u'(\lambda,\phi,z,t)\right)^2\right]. \quad (3)$$

These fields provide a measure of how regularly or how strongly the local meteorology varies from the local diurnal mean cycle. In Figure 9, the regions with the largest RMS values are favored locations for transient eddy activity.

[41] At $L_s = 120$ the transient activity appears primarily in the polar region, essentially along the edge of the NPRC. By $L_s = 135$ the topography of Alba Patera and Tharsis appears to be connected to the excitation of transient activity along the northern slopes of Alba Patera. The transient circulations that form here can traverse the high northern latitudes and reach the NPRC, which may dynamically link the midlatitude atmosphere to the polar region. By $L_s = 135$, the transient activity seen along the residual cap edge at $L_s = 120$ has mostly subsided. Some of the largest RMS excursions at $L_s = 135$ occur along a "storm track" region of elevated activity between Alba Patera and the NPRC. Our simulations produce strong transient eddy circulations in this "storm track," which are suggestive of the large annular cloud structure observed in Mars Orbital Camera (MOC) imagery, as described by *Cantor et al.* [2002]. By $L_s = 150$ the circulation has again changed dramatically, this time in response to the formation of an early fall polar jet, as seen in the zonal-mean zonal wind field of Figure 5a. The maximum RMS temperature excursion amplitude seen at $L_s = 150$ in Arcadia Planitia exists in connection with a maximum in this polar jet.

[42] Discussing the transitions in the zonal-mean and diurnal mean circulations, within the context of a rapidly changing insolation environment, allows some understanding of what is causing the polar circulation to change so quickly during this relatively short seasonal period. At $L_s = 120$ the sun is still well above the polar horizon, maintaining much warmer surface temperatures just off the NPRC. Analysis of the temperature data presented in Figure 8 shows that the meridional decrease in air temperature near the surface (from just off the cap edge to the pole) is ~5 K greater at $L_s = 120$ than at $L_s = 135$. The temperatures over the cap decrease less during this period than do those just off the cap, which causes the amplitude of the meridional temperature gradient to decrease. The weak jet that is observed over the edge of the residual cap (see Figure 5a or Figure 8) is related to the steeper gradient in atmospheric temperature at $L_s = 120$. Strong coriolis torques at these latitudes steer the off-cap katabatic flow into anticyclonic circumpolar easterlies near the surface. With the fairly sharp vertical wind shears that result, and the asymmetric topography of the NPRC, perturbations can develop at lower levels. The location and relative strength of these eddies can be seen in Figure 9. Flow from Chasma Boreale is important; interactions between circulations produce the region of enhanced activity ($\overline{u}'$) that is seen at the outlet of Chasma Boreale and additionally southeast of the outlet ($\overline{v}'$, $\overline{T}'$). Zonal asymmetry in the topography of the NPRC appears to be an important factor in the longitudinal preference of transient eddies at $L_s = 120$.

[43] By $L_s = 135$, the steepest northward facing slopes on the poleward side of the Tharsis and Alba Patera massif are receiving significantly less insolation. The diurnal surface temperature cycle in this region is large because the thermal inertia of this region is quite low. Both of these factors will enhance nocturnal drainage flows, which are already expected to be significant due to the topography of the region. Thus stronger drainage flows are able to influence the weather further poleward. The thermal low-pressure circulation over Alba Patera and Tharsis has weakened significantly, as seen in Figure 6 with the decreased strength of the counterclockwise circulation. Of interest is the fact that the poleward flow on the eastern slopes of Alba Patera and Tharsis has not diminished significantly in strength (presumably due to enhanced slope flows and western boundary current effects). We suggest that these factors are all involved in causing a favorable environment for transient circulations to form on the northern slopes of Alba Patera. These simulations also suggest that this favorable environment is short lived. The resulting activity on the northern slopes of Alba Patera and Tharsis is clearly seen in Figure 9. The transient eddies that form here can become quite large and they can traverse the distance to the NPRC, dynamically connecting the midlatitude atmosphere to the polar region (as discussed in greater detail below).

[44] Seasonal changes in the large-scale circulation and temperature structure by $L_s = 150$ continue to produce dramatic changes in the polar circulation, which is rapidly approaching winter-like conditions. An important component of these changes is the stronger flow that exists in relation to Elysium Mons. As seen in Figure 6, the diurnal mean winds near Elysium Mons strengthen between $L_s = 135$ and $L_s = 150$; this aspect of the diurnal mean circulation is now influencing the polar region. Additionally, the mean excursion amplitudes related to the flow near Elysium Mons (Figure 9) have strengthened significantly and now reach into the polar region, allowing transient circulations to dynamically connect the midlatitude atmosphere near Elysium Mons to the polar latitudes. This transition may be similar to what was seen with Alba Patera and Tharsis between $L_s = 120$ and $L_s = 135$, although it is occurring later due to the more southerly latitude of Elysium Mons. The largest amplitude in the RMS temperature excursion field at $L_s = 150$ in Figure 9 is related to a maximum in the zonal-mean zonal jet as seen in Figure 5a. The collocation of these features is good evidence that stronger baroclinic transients have become commonplace by $L_s = 150$. This early fall jet actually has two maxima, one north of Elysium Mons and the other north of Alba Patera (the stronger of the two). The spatial structure of this jet is depicted in Figure 10 for nine levels in the atmosphere, from ~18 km down to ~1 km. This jet forms primarily in response to the steepening meridional gradient in atmospheric temperature at ~65°N (see Figure 5a); however, Figure 10 appears to suggest that flows near the topography of Elysium Mons and near Alba Patera and Tharsis are involved in the longitudinal preference of the jet maximums, possibly in relation to the poleward transport of midlatitude air with greater angular momentum. Concerning Alba Patera and Tharsis, strong transient circulations continue to form and move northward, although these transient eddies now follow paths that are directed more eastward.

[45] A primary motivation for this work was to develop a model that can be used to refine our understanding of the

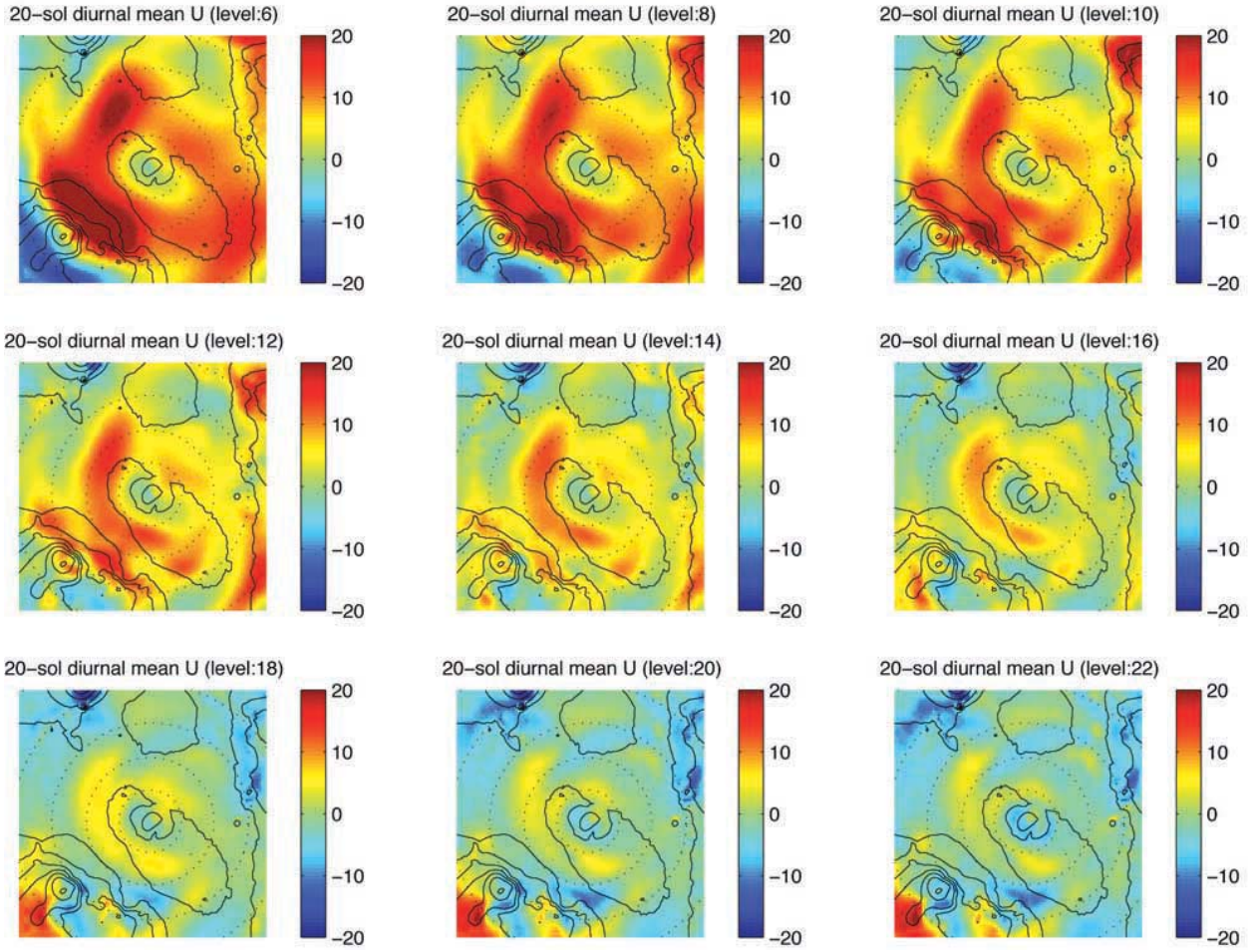

Figure 10. The diurnal mean zonal wind field at $L_s = 150$ is shown for 9 sigma levels (a 20-sol mean). Sigma level 6 is ~18 km, level 10 is ~10 km, level 14 is ~6 km, level 18 is ~3 km, and level 22 is ~1 km.

annual water cycle, specifically that of the NPRC. Even with a dry atmosphere in the present model configuration, some information concerning the meridional transport and mixing of water vapor can be deduced from dynamics alone. Transient circulations are important in the poleward fluxes of heat and momentum; and, although these quantities are by no means passive tracers, their values do provide some qualitative assessment of pathways in the atmosphere that may be important in the meridional transport of water vapor. Time histories of momentum and heat fluxes are constructed from the excursion records of U, V and T. We again examine 20-sol mean quantities; mean fluxes were constructed for each simulation of this study and the maps of 20-sol mean values are shown in Figure 11. The mean transient eddy momentum flux and the mean transient eddy heat flux are defined as follows:

$$\overline{u'v'}(\lambda,\phi,z) \equiv \sum_{t=1}^{t=N}\left(\frac{1}{N}\right)(u'(\lambda,\phi,z,t))(v'(\lambda,\phi,z,t)); \quad (4)$$

$$\overline{v'T'}(\lambda,\phi,z) \equiv \sum_{t=1}^{t=N}\left(\frac{1}{N}\right)(v'(\lambda,\phi,z,t))(T'(\lambda,\phi,z,t)). \quad (5)$$

[46] The transient eddy fluxes of heat and momentum at $L_s = 120$ provide further insights into how and where the eddies form and develop along the edge of the NPRC. The heat fluxes are strongest near the outlet of Chasma Boreale (where the katabatic flows are the strongest), whereas the momentum fluxes tend to be largest in some of the same regions in which the excursion winds are largest, along the edge and over the NPRC. The fact that the heat fluxes are sizeable and mostly positive (poleward) around the NPRC is certainly suggestive as to the possible role of baroclinic instability in the development of these eddies. The winds associated with the eddies at $L_s = 120$ often blow directly over the polar cap itself (as will be seen in detail in the next section), due to the dominant zonal wave number one structure which is present. These over-the-cap winds should be particularly effective in rapidly "ventilating" the cap interior (removing the saturated low-level air and bringing in warmer, potentially unsaturated, air). Because of this, and the direct influence of strong surface winds upon ice sublimation rates, the transient eddy circulations at $L_s = 120$ seem likely to be of considerable importance in the water cycle of the NPRC. The polar eddy winds should contribute to producing larger net sublimation rates than would exist in

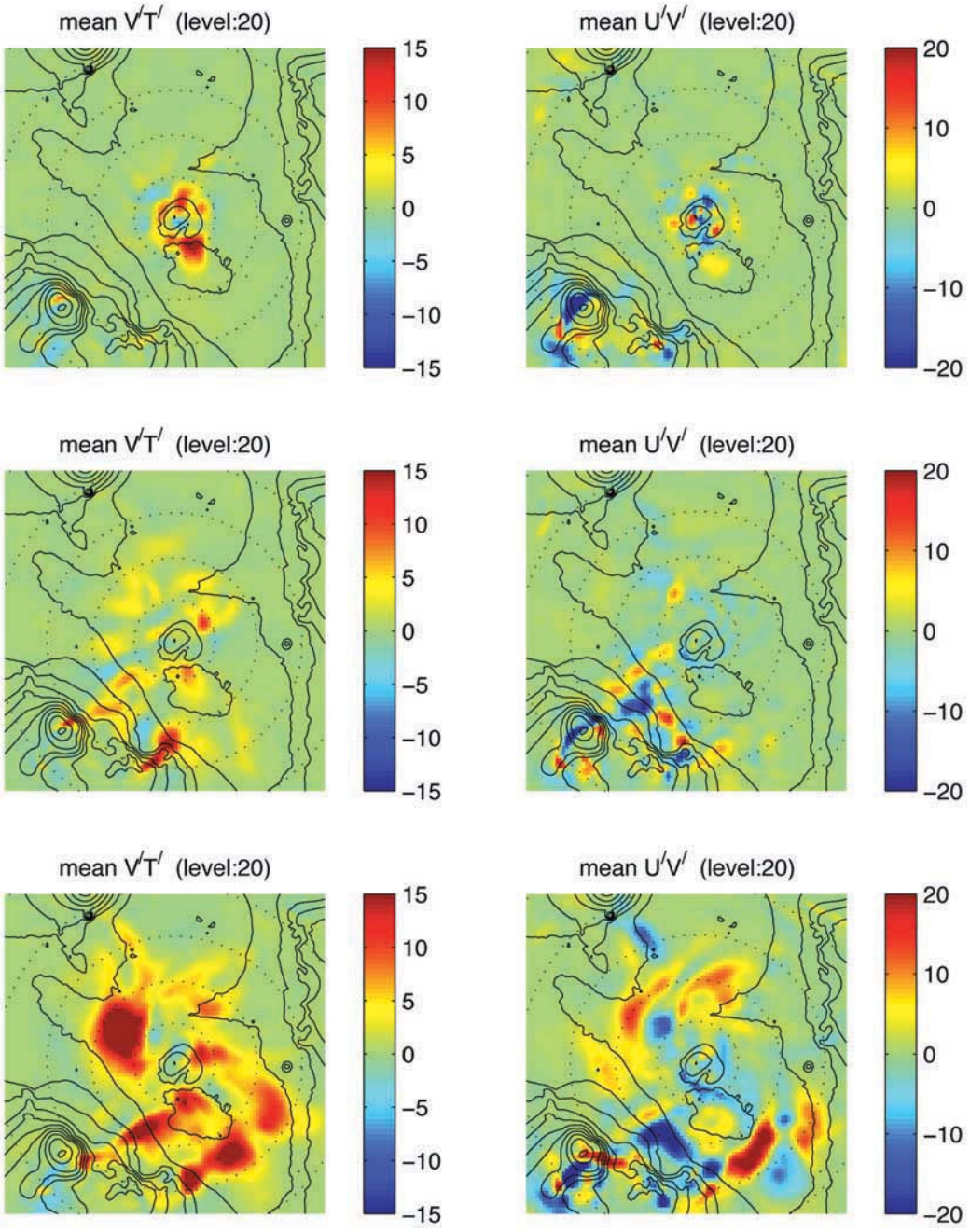

Figure 11. The 20-sol means of the eddy momentum flux ($\overline{u'v'}$) and the eddy heat flux ($\overline{v'T'}$) are shown for L_s = 120, L_s = 135, and L_s = 150, from top to bottom.

their absence. The time-mean circulation is important also, but the timescales on which it can act to "ventilate" the NPRC atmosphere (~5–10 sols) are significantly longer than those on which the polar eddies can act (~1 day) to do this.

[47] The heat and momentum fluxes at L_s = 135 lend further support to the picture outlined above of an eddy "storm track" extending from the northern slopes of Alba Patera and Tharsis to the NPRC. The detailed synoptic views of the eddy structure in the next section make it very clear that this is indeed a storm track region, in which the eddies form on the northern slopes of the Alba Patera and Tharsis massif, develop, and propagate poleward, before finally decaying in the vicinity of the NPRC. The detailed dynamics of this storm track region are not clear at present; they do not appear to be associated with conventional baroclinic instability. They do appear to be linked to strong low-level flows in this region (slope and other flows, as discussed above), and perhaps are tied rather directly to the huge topography. This storm track is very prominent at this seasonal date in the mesoscale simulations and basically absent in the L_s = 120 period, though it is present in somewhat altered form in the L_s = 150 simulation as discussed below.

[48] The existence of this storm track region is certainly intriguing in the context of possible water transports between the NPRC and middle latitudes during the summer. Explicit water transport simulations with a mesoscale model are needed to really address this issue, and such simulations are now being pursued. In the absence of results from such simulations, the impact of the L_s = 135 storm track on water transports and the polar water cycle can only be speculated upon. It is certainly very interesting that *Benson et al.* [2003] have found a large increase in clouds around Alba Patera at this season, in addition to an earlier seasonal peak at Ls $\sim$ 60 which is almost certainly associated directly with the retreat of the seasonal CO_2 polar cap. *Cantor et al.* [2002] have presented observations by both the MGS MOC and Hubble Space Telescope of very large annular cloud structures at nearly this same season, in the same region as the storm track in this simulation. In the next section, further details of the actual eddy structures at L_s = 135 will be presented and will be seen to be quite consistent with the Cantor et al. observations. It seems certain that the vigorous transient eddy activity found in the mesoscale simulations here must be of considerable importance for the summertime behavior of water in the northern polar region.

[49] By L_s = 150 the atmospheric circulation at high latitudes has begun to look very winter-like. A strong dynamical connection remains between the polar region and the northern slopes of Tharsis and Alba Patera. By this date Elysium Mons is also exhibiting a dynamical link to the polar region through transient eddies. Significant meridional transport of heat is taking place along the rapidly intensifying polar jet, suggesting strong baroclinic activity in the atmosphere. Our treatment of atmospheric dust at this time is less realistic than for the earlier two simulations; however, a more realistic treatment of dust would almost certainly sharpen the meridional decrease of atmospheric temperature and strengthen the development of winter-like circulations and baroclinic activity.

3.2.1. Surface Pressure Excursions

[50] Before looking at the actual instantaneous structure of the circulations that cause certain regions to have larger RMS excursion values, along with significant eddy momentum and heat fluxes, it is instructive to examine RMS excursions from the mean local diurnal cycle of surface pressure. Since topographical variation affects surface pressure on Mars so dramatically, it also affects the amplitude of surface pressure excursions as transient eddies move along topographical gradients. However, this bias can be removed by normalizing surface pressure excursions with the local diurnal mean surface pressure, yielding normalized surface pressure excursions. As with sea-level pressure and terrestrial cyclones, normalized surface pressure excursions are extremely effective for locating transient eddies that possess significant vorticity on Mars.

[51] To construct realistic excursion amplitudes for a 20-sol period, the mean hourly diurnal surface pressure cycle is trended with a function that has a mean value of unity, $\alpha(t)$; this is a low-order polynomial fit to a 20-sol record of the hourly domain mean surface pressure record, which is then divided by the value of the 20-sol domain mean surface pressure (forcing the mean value of $\alpha(t)$ to be unity). Multiplying the hourly mean diurnal cycle of surface pressure by this function simulates seasonal drift in the hourly mean diurnal cycle of surface pressure, eliminating systematic errors in the records of surface pressure excursions. These 20-sol records of normalized surface pressure excursions, expressed as percentages, are constructed as follows:

$$P'_{sfc}(\lambda,\phi,t) \equiv 100 \times \left(P_{sfc}(\lambda,\phi,t) - \alpha(t)\overline{P}_{sfc}(\lambda,\phi,hr)\right) \cdot \left(\overline{P}_{sfc}(\lambda,\phi)\right)^{-1}. \quad (6)$$

Using these records, the RMS surface pressure excursion field is constructed as with all of the RMS quantities described above:

$$\overline{P}'_{sfc}(\lambda,\phi) \equiv \mathrm{SQRT}\sum_{t=1}^{t=N}\left[\left(\frac{1}{N}\right)\left(P'_{sfc}(\lambda,\phi,t)\right)^2\right]. \quad (7)$$

The resulting fields are shown in Figure 12. The top two subplots both show results for L_s = 120 (two resolutions are shown, for the 54 km and 18 km nests); the bottom subplots show results from the L_s = 135 and L_s = 150 cases for the 54 km nest. As expected for L_s = 120, transient eddy pressure variations are most prominent along the edge and over the NPRC, with a region of strong activity that reaches southward from the mouth of Chasma Boreale to $\sim$70°N. A 20-sol mean amplitude of $\sim$0.75% is sizeable, since excursions of $\sim$1–2% are dynamically similar to terrestrial synoptic disturbances. As seen above for L_s = 120, there is very little transient eddy activity on the northern slopes of Alba Patera and Tharsis, although the summit of Alba Patera itself shows activity in the 54 km nest. Immature eddies north of Alba Patera track westward, although they quickly decay in conditions that are apparently unfavorable for their growth; this may be a consequence of the stronger thermal low-pressure circulation at this time, although the dynamics are not yet understood. At L_s = 135 we again see the basic result as described above, a "storm track" connects the atmosphere over Alba Patera and Tharsis to the polar region. Transient eddies, which form on the shoulder of Alba Patera and Tharsis, grow and move poleward before they decay at the edge of the NPRC. At L_s = 150 the transient eddies that form on Alba Patera and Tharsis do so to the east of the summit, and track poleward with a more eastward path. We believe that a favorable mix of circulations occurs for a short period at $L_s \sim$ 135, which allows the formation of this "storm track." We do not fully understand the complicated mix of dynamics that is involved at this time, although the diurnal mean winds at L_s = 135 (Figure 6) suggest that energy is being removed from the mean flow along the northern slopes of Alba Patera. This state does seem to be a transition one that is fairly short lived. As described above, this transitory state may be favorable for the appearance of the second peak in Alba Patera cloud areas found by *Benson et al.* [2003] and the large annular cloud structure described by *Cantor et al.* [2002]. The development of the polar jet by L_s = 150 (Figure 5a and Figure 10) is directly involved in the increase in the mean strength of the transient eddies seen at this time; intense

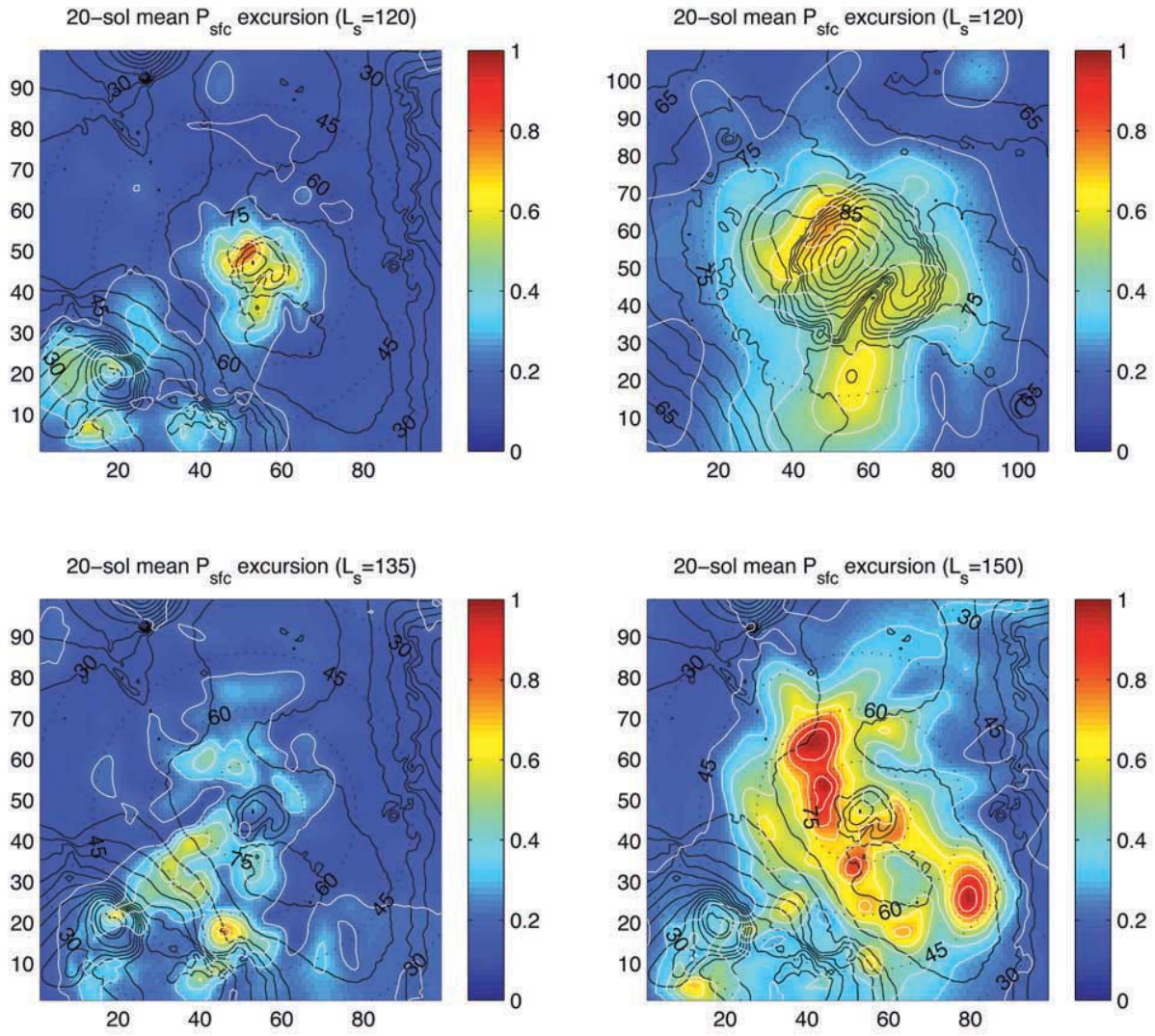

Figure 12. The 20-sol RMS normalized excursions from the mean diurnal surface pressure cycle are shown (as percentages). The top two subplots show the L_s = 120 case for both the 54 km and 18 km nests; the bottom subplots show the L_s = 135 and L_s = 150 cases. Topography is contoured with solid black lines. Color shows the percentage amplitude of the 20-sol mean normalized surface pressure excursion (white lines contour the RMS excursions).

baroclinic processes are becoming prominent and summer has largely ended by L_s = 150 in the polar region.

3.2.2. Synoptic Eddy Structure

[52] The results described above suggest that transient eddies are prominent in the short northern polar summer and that they appear preferentially in favored locations that vary significantly with season. These transient circulations are excited and maintained by various mechanisms in a complex way that is caused by seasonal changes in the larger-scale circulation. Better insight into the dynamics can be gained through examination of the actual synoptic structures and evolution of the transient eddies. In this section the instantaneous wind excursions are presented, overlaid on the instantaneous surface pressure excursions, providing a clearer picture of the strength, structure and lifetime of the transient eddy circulations.

[53] In Figure 13 we examine the 18 km nest of the L_s = 120 case, showing the excursion wind field at every other grid point for σ = 20 ($\sim$1.5 km altitude), along with the surface pressure excursion field, for six times. Successive subplots are exactly one sol after the previous subplot, allowing for some visualization of the evolution of individual eddies over this 5-sol period. The excursion surface pressure field exhibits a pronounced zonal wave number one structure between $\sim$75 N and $\sim$85 N. The high and low centers of pressure have amplitudes reaching $\sim$1% and are generally oriented along the edge of the NPRC, separated in longitude by $\sim$180°. The excursion surface pressure centers exhibit a retrograde motion (east to west) along a weak and relatively low-level westerly jet, which is underlain by easterly mean flow (see Figure 5a and Figure 8). The transient eddies associated with the zonal wave number one structure are the largest, with spatial scales between $\sim$500 km and $\sim$1000 km; smaller eddies in the flow are also resolved by the model, with spatial scales for the surface pressure field of $\sim$100 km. An examination of all 20 sols of

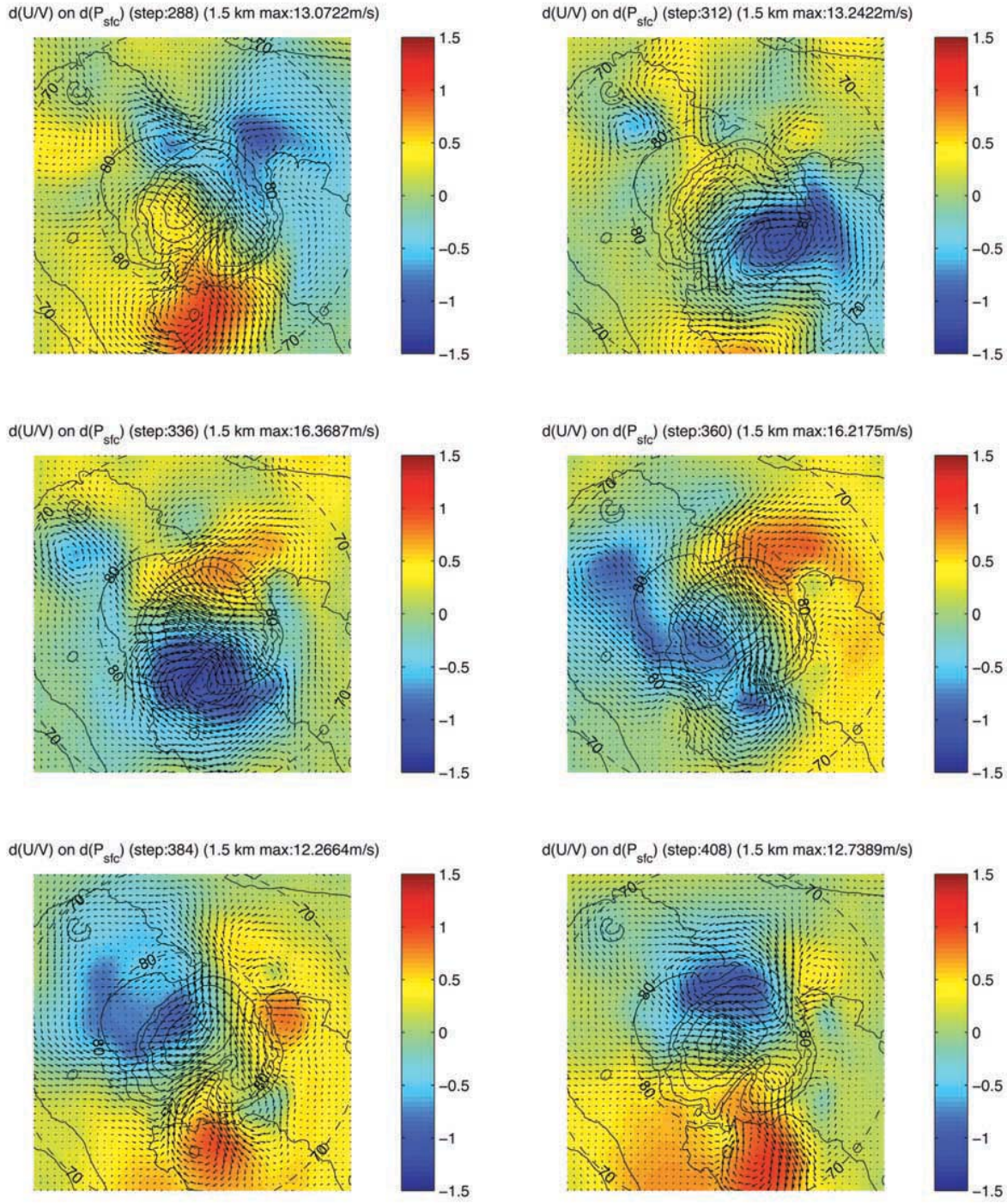

Figure 13. Six snapshots from the $L_s = 120$ simulation are shown. UTC time is 0 Z, and each subplot is one sol later than the previous. Color shows the instantaneous percentage deviation from the local surface pressure cycle. The arrows show the instantaneous wind excursions from the mean diurnal wind cycle (shown at every other grid point).

model output shows that the circulation can vary significantly from this zonal wave number one structure, although a single-point correlation analysis clearly shows that this structure is the dominant one (not shown). The retrograde propagation can be seen in Figure 13 by tracking the largest individual eddies to the west along the edge of the cap. The strongest excursion winds occur at the sharpest surface pressure gradients (directly between the high- and low-pressure centers); these winds can be strong (~15 m/s), and due to the zonal wave number one structure they blow directly and consistently across the central region of the NPRC. The structure of this circulation is constantly changing; flows associated with Chasma Boreale play an important role in causing the largest variations, appearing to

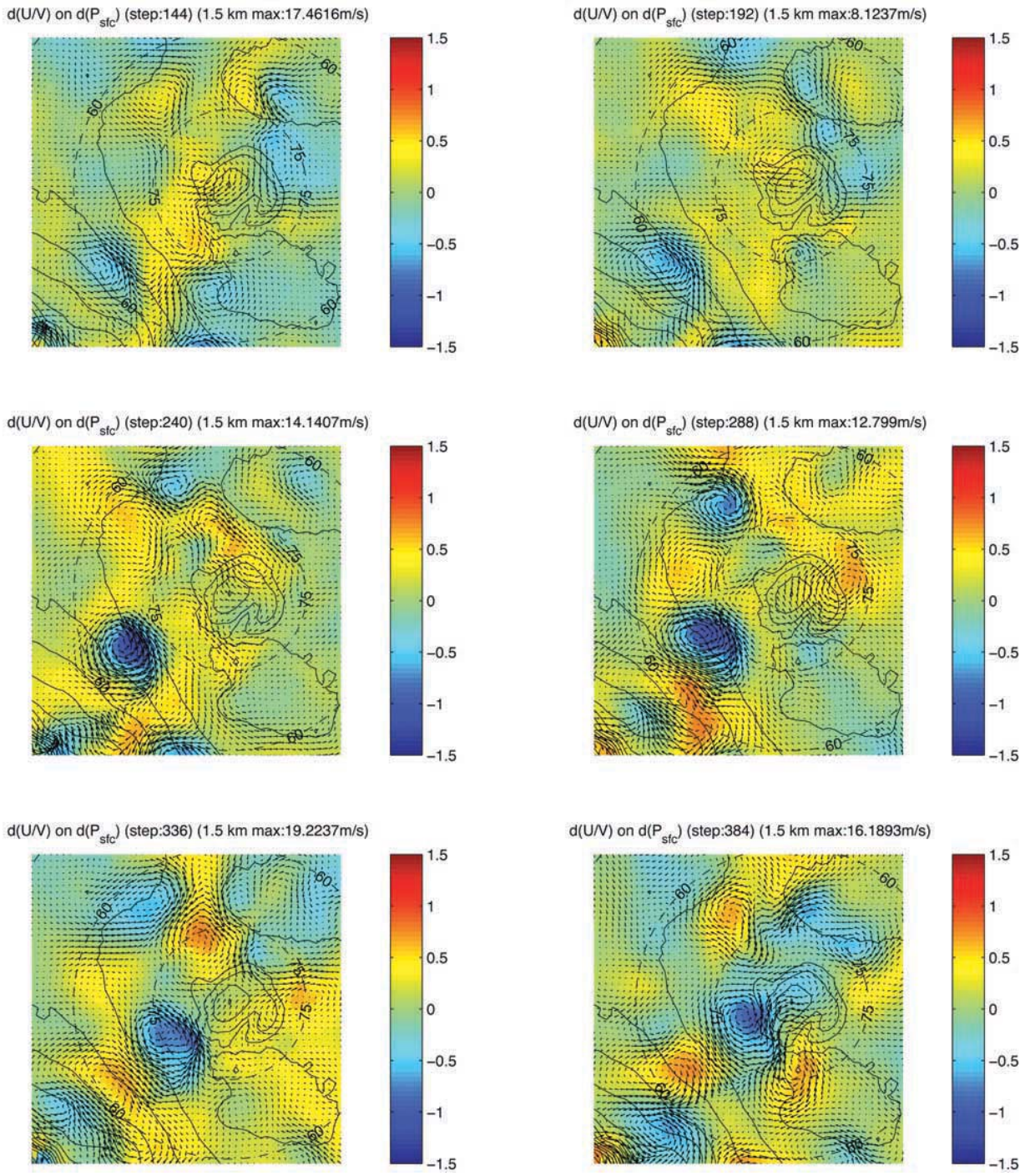

Figure 14. Six snapshots from the L_s = 135 simulation are shown. UTC time is 0 Z, and each subplot is two sols later than the previous. Color is the instantaneous percentage deviation from the local surface pressure cycle. The arrows are the instantaneous wind excursions from the mean diurnal wind cycle.

alternatively enhance or diminish the surface pressure centers and winds. For this L_s = 120 case, a lagged single-point correlation analysis shows that the circumpolar transit time (the period) of this zonal wave number one structure is ~5 sols.

[54] In Figure 14 we examine the structure of transient eddies for a subset of the 54 km nest in the L_s = 135 case, plotting instantaneous excursion winds for $\sigma = 20$ (~1.5 km) on the instantaneous surface pressure excursions. The subplots in Figure 14 show six times and successive subplots are exactly two sols apart. In the bottom left corner of the first subplot a cyclonic eddy has formed on the flanks of Alba Patera and Tharsis. This eddy grows much deeper and travels northward along the "storm track" that has been described above, lasting for ~10 sols until it reaches the NPRC and dissipates its energy. This

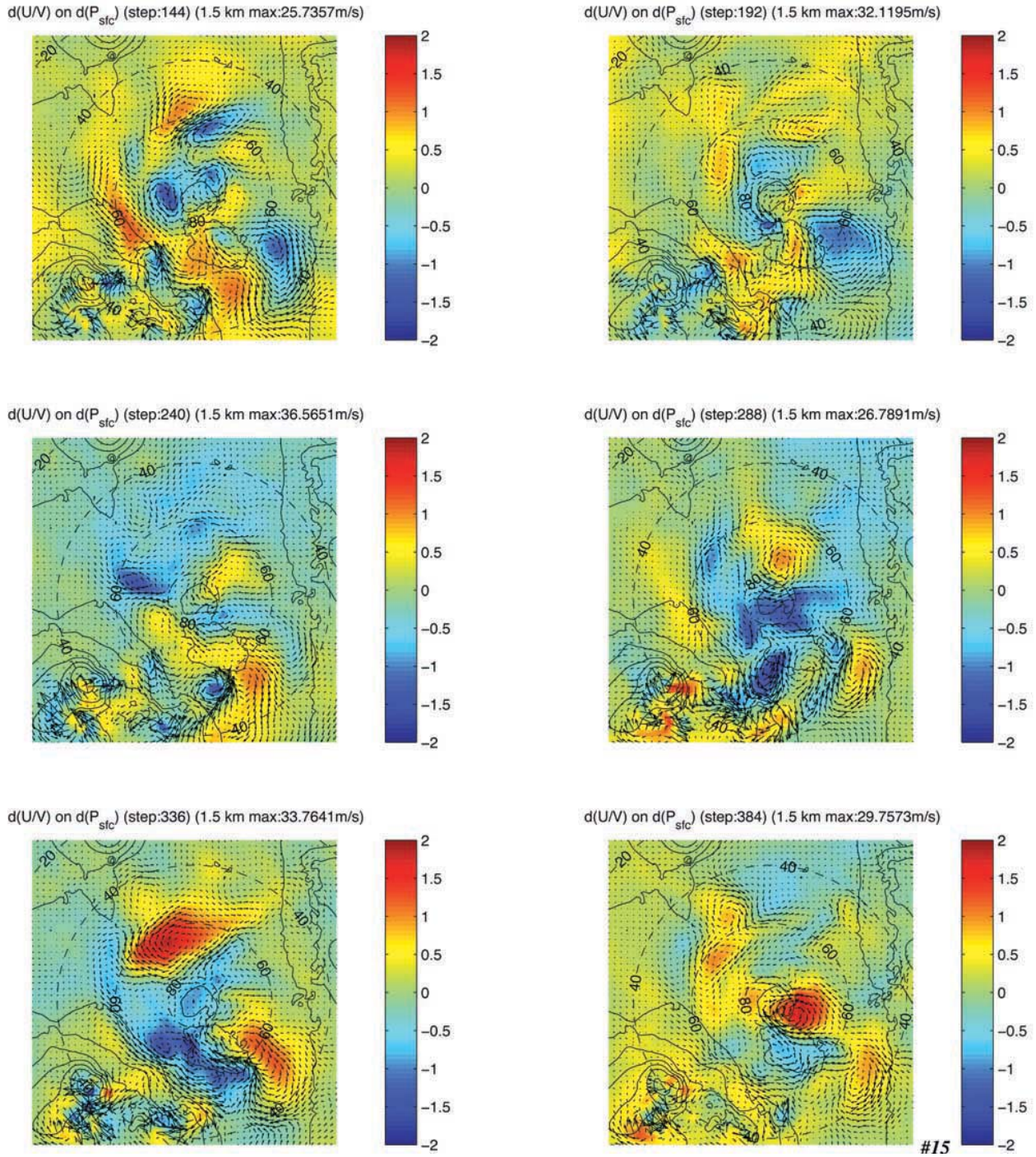

Figure 15. Six instants from the L_s = 150 simulation are shown. UTC time is 0 Z, and each subplot is two sols later than the previous. Color shows the instantaneous percentage deviation from the local surface pressure cycle (note the wider color bar than for L_s = 120 and L_s = 135). The arrows are instantaneous wind excursions from the mean diurnal wind cycle (shown for every other grid point).

eddy is surprisingly long-lived, strong (fractional surface pressure excursions of ~1.5% with excursion wind speeds of ~15 m/s) and traverses a large meridional distance. At the end of this sequence it can be seen that another such eddy is forming in the same location, suggesting that a recurring "cycle" of formation, growth, poleward migration and dissipation over the NPRC occurs during this portion of the midsummer season. The large transient eddy seen in Figure 14 travels northward ~35° of latitude in a 10 sol period, averaging ~2 m/s. At time step 240 in Figure 14 it is in a strong developmental phase with a clear frontal boundary evident in the wind field; a diurnal cycle of relative growth and decay is seen when all hours of the day are examined, consistent with the observations

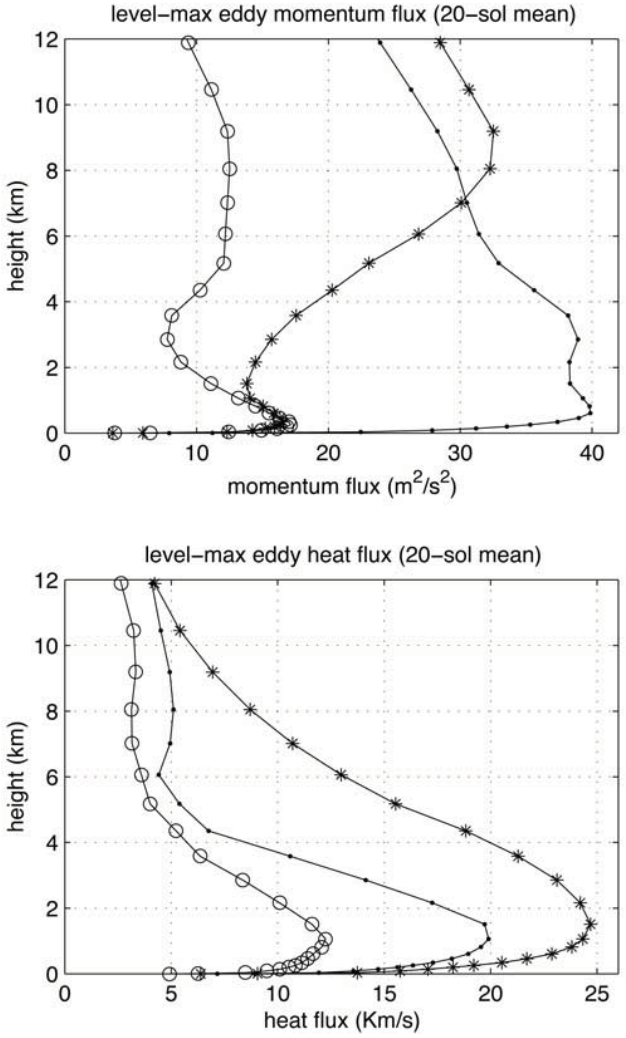

Figure 16. Level maximum profiles are shown. These profiles were constructed from the 20-sol mean fields of eddy heat flux and eddy momentum flux in the 18 km nest. Profiles are shown for each of the three simulations in this study; the lines are marked with dots, circles, and asterisks to indicate the L_s = 120, L_s = 135 and L_s = 150 simulations, respectively.

of summer polar eddies by *Cantor et al.* [2002]. Meridional mixing of the atmosphere will occur in response to the excursion winds of such large eddy circulations (roughly as large as the NPRC itself). As noted above, this ''storm track'' corridor may be important in the transport of water vapor into lower latitudes at $L_s \sim 135$ and may provide water vapor to enhance cloud formation over Alba Patera [*Benson et al.*, 2003]. Other long-lived and large eddies do form at ~70°N between ~90°E and ~180°E, and these circulations would contribute to meridional mixing of the atmosphere. Much weaker eddies with retrograde motion can still be seen to form along the edge of the NPRC, although these have mostly disappeared, as has the weak westerly jet over the cap edge.

[55] In Figure 15 we examine the L_s = 150 case for the 54 km nest, showing the excursion wind field at every other grid point for σ = 20 (~1.5 km) overlaid on the surface pressure excursion field (successive subplots are exactly two sols later). The L_s = 150 circulation is more complex than that of the earlier two dates. Besides forming in response to interaction between topographically excited circulations near the surface, transient eddies are now seen to form along an early fall polar jet at altitude (see Figure 10). Since these stronger winter-like eddies are becoming common by L_s = 150, the circulation over the polar region is affected and changes in the eddy heat and eddy momentum flux indicate that the strength of eddies at altitude is increasing. In Figure 16 vertical profiles of the level maximum values of the eddy momentum and eddy heat fluxes are plotted (data was taken from the 20-sol means of these two fields in the 18 km nest, significantly poleward of the developing jet). In the top subplot we see that the eddy momentum flux at L_s = 150 (asterisks) is largest at altitude, increasing dramatically with altitude in comparison to the other two cases. The largest eddy momentum fluxes are caused by eddies that develop near the surface at L_s = 120 (dots). The stronger eddies along the jet at L_s = 150 are equatorward of this domain, although they are apparently affecting the circulation at altitude over the pole (seen in Figure 15 and discussed below). The heat flux profiles all have a similar shape, although the change with season is not linear; Ls = 135 (circles) has the least eddy activity of all the three simulations (the most summer-like). For L_s = 120 and L_s = 135 the eddy heat flux is strongest at ~1.5 km but has dropped off to background noise levels by ~4 km. For L_s = 150 the peak occurs somewhat higher and values do not drop off to background levels till ~10 km. Although near surface circulations are still causing eddies to form at L_s = 150, the affect of the developing jet at lower latitudes is being seen over the polar region.

[56] Transient eddies at L_s = 150 can become much stronger (a wider color bar is used in Figure 15 than in Figure 13 or Figure 14); they have surface pressure excursion amplitudes that can reach ~2% (dynamically equivalent with mature terrestrial cyclones). As seen in the bottom left of each subplot shown in Figure 15, the circulation near Alba Patera is highly complex and time variable. Eddies that form on Alba Patera and Tharsis track toward the NE and cross the NE shoulder of Tharsis as they move into northern Acidalia Planita. The results of this eddy activity are clearly reflected in the mean heat and momentum fluxes of Figure 11. The L_s = 150 case of Figure 12 puts an important constraint on the location of the strongest eddies seen in Figure 15; the path they tend to follow is an elongated ellipse in this domain (this is best seen in animations). As seen in Figure 15 at time steps 288 and 384, the pole can be affected by either a significant low-pressure or high-pressure disturbance (deeper eddies at altitude, as in Figure 16). Step 336 gives an example of the size of an individual transient eddy (~1500 km) that is contributing to the maximum values in the mean eddy heat flux in Figure 11.

4. Estimation of Water Vapor in the Polar Atmosphere

[57] Water vapor is not an active tracer in the simulations performed in this study; however, we can use the modeled temperature and density profiles over the cap to construct an

estimate of the amount of water the atmosphere would hold if it were saturated with respect to water ice. To quantitatively describe the rates involved in water processes a complete calculation is required, one that includes physics for the exchange of water vapor with the NPRC and the transport of water vapor in the atmosphere. The period between L_s = 120 and L_s = 150 is important in the annual water cycle, especially the water cycle of the NPRC; TES data show that there is a dramatic and rapid decrease in the amount of water in the polar atmosphere during this period; it is an open question whether the bulk of this water is transported equatorward or whether it again becomes part of the NPRC.

[58] Surface and atmospheric temperatures change rapidly during this short seasonal period, and this is reflected in the amounts of water vapor the atmosphere can hold at saturation. With respect to the persistence of transient eddy activity observed in these simulations over the NPRC, surface winds may be very important in determining the amount of water sublimated from the NPRC.

[59] To approximate the saturation vapor pressure for water over ice (e_{sat}) in the Martian atmosphere we use the prescription adopted by *Richardson and Wilson* [2002], given below in millibars for atmospheric temperatures (T) in Kelvin:

$$e_{sat} = 6.11 \times \exp\left[22.5 \times \left(1 - \frac{273.16}{T}\right)\right]. \quad (8)$$

The saturation density profile of water vapor in the atmosphere is determined from the mixing ratio at saturation (w_{sat}):

$$\rho_v = \rho_d \times w_{sat} = \rho_d \times \frac{R_d}{R_v}\left(\frac{e_{sat}}{p - e_{sat}}\right). \quad (9)$$

The quantities R_d and R_v are the gas constants for Martian air and water vapor; their ratio is 0.416. To determine the total mass of water vapor in the atmospheric column the hydrostatic equation is used to determine the thickness of individual layers, and then a sum over all layers provides the total mass of water vapor in the unit column:

$$\frac{M_v}{A} = \sum_z \rho_v dz = \sum_z \rho_v \times \left(\frac{-dp}{\rho g}\right). \quad (10)$$

When divided by the density of liquid water the result is then expressed as a thickness; the results given below are in precipitable microns (pr-μm), for comparing with the TES observations of *Smith* [2004].

[60] For the three simulations in this study a diurnal average temperature profile was constructed for a small region over the NPRC, a region that is essentially poleward of ~85°N. In a saturated atmospheric profile nearly all of the water exists at elevations lower than ~15 km above the surface. Since the vertical depth of the transient circulations in these simulations scales within the first pressure scale height, vertical mixing should also be greatest below ~15 km. With advancing season there is a very rapid decrease in the amount of water vapor that can be held in a saturated atmospheric column. At L_s = 120, L_s = 135 and L_s = 150, the simulated atmosphere over the NPRC can respectively hold 51 pr-μm, 25 pr-μm and 9 pr-μm. At L_s = 120 the agreement with the TES data appears to be fairly good; the amount of water in a saturated model column does appear to decrease somewhat more quickly than in the TES observations of *Smith* [2004]. The temperature profile of the lowest ~2 km in the model affects these results quite significantly.

5. Summary and Discussion

[61] The OSU Mars MM5 has been used to perform the first comprehensive study of summertime atmospheric circulations at high resolution over the northern polar region. To provide an accurate thermal environment for the highest latitudes (so that atmospheric dynamics are realistically forced), we have extrapolated the TES derived thermal inertia data of *Putzig et al.* [2005] to the pole. Our method (guided by some simplifying assumptions) assumes that poleward of 80°N there is a good correlation between thermal inertia and surface albedo; our maps resemble the thermal inertia data of *Paige et al.* [1994]. Using these data our modeled surface temperatures for the residual cap and the surrounding region agree relatively well with MGS/TES observations of surface temperature (Figure 3); atmospheric temperatures were tuned to match a zonal-mean MGS RS temperature profile by adjusting the optical depth of atmospheric dust. Overall, the representation of the observed polar thermal environment is quite good, giving us confidence that the model dynamics are realistic.

[62] These simulations are performed hydrostatically; and the model atmosphere is assumed to be dry with a globally uniform distribution of dust. Hydrostatic dynamics significantly reduce computational requirements and have allowed for the testing of numerous domain configurations, a tuning of the model to data and a suite of three long simulations (29 sols each). The simulations in this study span a summertime period as defined by three solar longitudes: L_s = 120, L_s = 135 and L_s = 150. The final 20 sols of output from each simulation are centered on these dates and have been used to generate model statistics. It is central to this study that this approach has allowed the extraction and examination of transient eddy circulations. The seemingly long period allocated to model spin-up (total of 9 sols) is required in part due to the modified polar surface thermal properties used in these simulations. However, model time is always needed for soil temperatures to reach equilibrium; and, model time is needed for the larger-scale circulations, that are not well represented in the GCM initial conditions, to fully develop and adjust to the higher-resolution topography being used in the model. The highest-resolution nest activated in this study has a nominal resolution of 18 km; this domain includes the north residual ice cap and the surrounding region poleward of ~70°N (surface properties are shown in Figure 1 and Figure 2).

[63] Summertime circulations in the northern polar region vary dramatically between L_s = 120 and L_s = 150. At L_s = 120 transient eddies form continuously along the edge of the residual cap. These eddies have strong excursion winds (~10–15 m/s) that blow directly across the cap throughout this simulation. The existence of these transient eddies

and the surprisingly strong winds suggests the following: (1) there is a vigorous vertical mixing of water vapor along the cap edge that is driven by these circulations, (2) water vapor (sublimated ice) is quickly transported away from the cap surface, and (3) enhanced sublimation of ice from the NPRC occurs due to the regular influx of warmer off-cap air over the NPRC and the strong eddy winds. The transient eddies at L_s = 120 exhibit a dominant zonal wave number one structure around the residual cap. They have a retrograde motion with a period of ~5 sols along a weak westerly jet underlain by surface easterlies. These transient circulations are contained within the first pressure scale height (~10 km) above the surface.

[64] At L_s = 135, in response to changes in the large-scale circulations over Alba Patera and on the northern slopes of Tharsis, strong and long-lived transient circulations form that can traverse the northern latitudes and reach the residual cap. These circulations appear to dynamically connect the atmosphere of the midlatitudes to that of the polar region. By this date the relatively isolated structure of transient eddies over the NPRC has mostly ended; this is in part due to these strong eddies moving poleward through this ''storm track'' region to the edge of the NPRC. Other relatively strong eddies, that would enhance the mixing of water vapor are also seen to form at latitudes somewhat south of the cap. The zonal-mean overturning in the atmosphere over the NPRC is strongest at L_s = 135, and the mean circulation (the katabatic off-cap winds and associated easterlies) tends to dominate the circulation at the highest latitudes. There is no jet in the polar atmosphere at L_s = 135 as there is at L_s = 120, and the winter-like conditions of L_s = 150 have not yet developed. The polar circulation is in transition at this date.

[65] The ''storm track'' observed at L_s = 135 in this study provides a possible explanation for the two-peak distribution of water ice clouds over Alba Patera, as described by *Benson et al.* [2003], while suggesting that the rapid decrease of water vapor in the polar region occurring at this time could be partially caused by equatorward transport along this corridor. By $L_s \sim 135$, columnar mass abundances of water vapor over the polar region are in rapid decline [*Smith*, 2004]. The amount of water vapor that can be held in the atmosphere (under the assumption that saturation is an upper limit) is dropping rapidly with falling polar temperatures, as shown by the calculations of the previous section. Until high-resolution simulations can be performed that include the atmospheric transport of water vapor and realistic sublimation/deposition physics for the NPRC surface, the importance of water freed from the NPRC in the annual water cycle will remain a poorly constrained problem.

[66] Transient eddies observed in the L_s = 120 and L_s = 135 cases are primarily excited by strong near surface flows, and they are spatially related to topographically forced flows near the surface. The maximum amplitudes of the surface pressure excursions (transient eddies) at L_s = 120 and L_s = 135 are ~1% and ~1.5% respectively, dynamically scaling to somewhat weaker terrestrial cyclones. At L_s = 135 the modeled atmosphere is in a state of transition; the circulation does change somewhat over the 20-sol analysis period, whereas for the other two simulations the circulation is more steady over this period. Additionally, it is of interest to note that our analyses show statistically that the transient eddies have a significant diurnal variation in their amplitudes, even after the mean diurnal cycle has been removed in our construction of transient excursions. It seems clear that the diurnal cycle is important for the summer polar eddies. In the L_s = 135 simulation, a very large eddy forms poleward of the Alba Patera summit. This eddy is very similar in scale and location (being roughly as large as the NPRC) to eddies seen by both the Hubble Space Telescope and MGS/MOC [*Cantor et al.*, 2002] in multiple Mars northern summers, at about this same seasonal date.

[67] By L_s = 150 the polar atmosphere has cooled dramatically and the polar circulation is beginning to appear winter-like. An early fall polar jet has formed; it has a longitudinal structure that appears to be influenced by circulations that are associated with the topography of the Alba Patera and Tharsis massif and that of Elysium Mons. This jet has a zonal mean maximum of ~20 m/s. Baroclinic processes associated with this jet are clearly becoming important in forming strong transient circulations; surface pressure excursion amplitudes are much larger by this date (~2%). Additionally, the maximum amplitudes of the U, V and T excursions are seen to occur at greater altitude above the surface than at the earlier two dates, although these eddies are still contained within the first pressure scale height. The poleward eddy fluxes of heat and momentum are becoming quite significant by L_s = 150.

[68] It is important to again acknowledge that the dust distribution in the model at L_s = 150 is not as realistic as it could be. If dust were more realistically distributed in the model atmosphere at this time (decreasing with latitude) then the onset of stronger transient eddy circulations, and the development of the early fall jet, would tend to occur somewhat earlier and be stronger by L_s = 150. A more realistic dust distribution might also cause the transition period seen at L_s = 135 to occur somewhat earlier, although the dynamics of that transition are not clear at present. If so, the model might simulate the large annular cloud structures (large transient eddies in the ''storm track'') discussed by *Cantor et al.* [2002] somewhat earlier, in better agreement with observations.

[69] The period of this study (L_s = 120 to L_s = 150) is extremely important for the annual water cycle of the NPRC; this is when the columnar mass abundances of water vapor are observed to drop very sharply from the annual maximum. Activating additional physics in the OSU MMM5 for the surface exchange and atmospheric transport of water will improve our understanding of the important role that atmospheric dynamics plays in the polar region during northern summer. Moreover, such studies will allow better insight into the importance of NPRC water in the annual global water cycle. The upcoming Phoenix Mars Scout mission (landing in 2007) will yield much needed in situ meteorological observations from a high northern latitude location from late spring to summer. The upcoming Mars Reconnaissance Orbiter will provide improved measurements of atmospheric and surface temperatures, water vapor and ice abundances during northern summer, as well as for other seasons.

[70] As our understanding of the bigger picture develops, the nonhydrostatic version of our model may become an important tool in providing a more accurate depiction of the

structure and evolution of the strongest transient and mean circulations found in this study. Nonhydrostatic modeling, in carefully focused studies with increased computational capacity, should become very important for refining our understanding of the highly complex circulations and vigorous transient eddies found in this initial summertime study of atmospheric circulations in the northern polar region.

[71] **Acknowledgments.** We would like to thank John Wilson and one anonymous reviewer for their thoughts and numerous valuable suggestions. Additionally, the International Conferences on Mars Polar Science and Exploration and the NASA Ames Mars GCM community have been, and continue to be, invaluable in the advancement of this research.

References

Banfield, D., B. J. Conrath, P. J. Gierasch, R. J. Wilson, and M. D. Smith (2004), Traveling waves in the Martian atmosphere from MGS TES nadir data, *Icarus*, *170*, 365–403.

Barnes, J. R. (2003a), Planetary eddies in the Martian atmosphere: FFSM analysis of TES data, paper presented at the International Workshop: Mars Atmosphere Modeling and Observations, Cent. Natl. d'Etud. Spatiales, Granada, Spain, 13–15 Jan.

Barnes, J. R. (2003b), Mars weather systems and maps: FFSM analyses of MGS TES temperature data, paper presented at 6th International Conference on Mars, Calif. Inst. of Technol., Pasadena, Calif., 20–25 July.

Barnes, J. R., J. B. Pollock, R. M. Haberle, B. Leovy, R. W. Zurek, H. Lee, and J. Schaeffer (1993), Mars atmospheric dynamics as simulated by the NASA Ames general circulation model: 2. Transient baroclinic eddies, *J. Geophys. Res.*, *98*, 3125–3148.

Benson, J. L., B. P. Bonev, P. B. James, K. J. Shan, B. A. Cantor, and M. A. Caplinger (2003), The seasonal behavior of water ice clouds in the Tharsis and Valles Marineris regions of Mars: Mars Orbiter Camera observations, *Icarus*, *165*, 34–52, doi:10.1016/S0019-1035(03)00175-1.

Bottger, H., S. R. Lewis, P. L. Read, and F. Forget (2005), The effects of the Martian regolith on GCM water cycle simulations, *Icarus*, in press.

Boynton, W. V., et al. (2004), The Mars Odyssey gamma-ray spectrometer instrument suite, *Icarus*, *110*, 37–83.

Cantor, B., M. Malin, and K. S. Edgett (2002), Multiyear Mars Orbiter Camera (MOC) observations of repeated Martian weather phenomena during the northern summer season, *J. Geophys. Res.*, *107*(E3), 5014, doi:10.1029/2001JE001588.

Christensen, P. R., et al. (2001), Mars Global Surveyor Thermal Emission Spectrometer experiment: Investigation description and surface science results, *J. Geophys. Res.*, *106*, 23,823–23,871.

Dudhia, J. (1993), A nonhydrostatic version of the Penn State–NCAR mesoscale model: Validation tests and simulation of an Atlantic cyclone and cold front, *Mon. Weather Rev.*, *121*, 1493–1513.

Grell, G. A., J. Dudhia, and D. R. Stauffer (1994), A description of the fifth-generation Penn-State/NCAR mesoscale model (MM5), *NCAR Tech. Note NCAR/TN-398+STR*, Natl. Cent. for Atmos. Res., Boulder, Colo.

Haberle, R. M., and B. M. Jakosky (1990), Sublimation and transport of water from the north residual polar cap on Mars, *J. Geophys. Res.*, *95*, 1423–1437.

Haberle, R. M., M. M. Joshi, J. R. Murphy, J. R. Barnes, J. T. Schofield, G. Wilson, M. Lopez-Valverde, J. L. Hollingsworth, A. F. C. Bridger, and J. Schaffer (1999), General circulation model simulation of the Mars Pathfinder atmospheric structure investigation/meteorology data, *J. Geophys. Res.*, *104*, 8957–8974.

Herkenhoff, K. E., and J. J. Plaut (2000), Surface ages and resurfacing rates of the polar layered deposits on Mars, *Icarus*, *144*, 243–253.

Hinson, D. P., G. L. Tyler, J. L. Hollingsworth, and R. J. Wilson (2001), Radio occultation measurements of forced atmospheric waves on Mars, *J. Geophys. Res.*, *106*, 1463–1480.

Hinson, D. P., M. D. Smith, and B. J. Conrath (2004), Comparison of atmospheric temperatures obtained through infrared sounding and radio occultation by Mars Global Surveyor, *J. Geophys. Res.*, *109*, E12002, doi:10.1029/2004JE002344.

Houben, H., R. M. Haberle, and R. E. Young (1997), Modeling the Martian seasonal water cycle, *J. Geophys. Res.*, *102*, 9069–9083.

Howard, A. D. (2000), The role of eolian processes in forming surface features of the Martian polar layered deposits, *Icarus*, *144*, 267–288.

Hvidberg, C. S. (2003), Relationship between topography and flow in the north polar cap on Mars, *Ann. Glaciol.*, *37*, 363–369.

Jakosky, B. M. (1983), The role of seasonal reservoirs in the Mars water cycle, II, Coupled models of the regolith, the polar caps, and atmospheric transport, *Icarus*, *55*, 19–39.

Joshi, M. M., S. R. Lewis, P. L. Read, and D. C. Catling (1995), Western boundary currents in the Martian atmosphere: Numerical simulations and observational evidence, *J. Geophys. Res.*, *100*, 5485–5500.

Klemp, J. B., and R. B. Wilhelmson (1978), Simulations of three-dimensional convective storm dynamics, *J. Atmos. Sci.*, *35*, 1070–1096.

Michaels, T. I., and S. C. R. Rafkin (2004), Large-eddy simulation of atmospheric convection on Mars, *Q. J. R. Meteorol. Soc.*, *130*, 1251–1275.

Montmessin, F., F. Forget, P. Rannou, M. Cabane, and R. M. Haberle (2004), Origin and role of water ice clouds in the Martian water cycle as inferred from a general circulation model, *J. Geophys. Res.*, *109*, E10004, doi:10.1029/2004JE002284.

Paige, D. A., and A. P. Ingersoll (1985), Annual heat balance of Martian polar caps: Viking observations, *Science*, *228*, 1160–1168.

Paige, D. A., J. E. Bachman, and K. D. Keegan (1994), Thermal and albedo mapping of the polar regions of Mars using Viking thermal mapper observations: 1. North polar region, *J. Geophys. Res.*, *99*, 25,959–25,991.

Pollack, J. B., J. Schaeffer, and H. Lee (1990), Simulations of the general circulation of the Martian atmosphere: 1. Polar processes, *J. Geophys. Res.*, *95*, 1447–1473.

Prettyman, T. H., et al. (2004), Composition and structure of the Martian surface at high southern latitudes from neutron spectroscopy, *J. Geophys. Res.*, *109*, E05001, doi:10.1029/2003JE002139.

Putzig, N. E., M. T. Mellon, K. A. Kretke, and R. E. Arvidson (2005), Global thermal inertia and surface properties of Mars from the MGS mapping mission, *Icarus*, *173*, 325–341.

Rafkin, S. C. R., M. R. V. Sta. Maria, and T. I. Michaels (2002), Simulation of the atmospheric thermal circulation of a Martian volcano using a mesoscale numerical model, *Nature*, *419*, 697–700.

Richardson, M. I., and R. J. Wilson (2002), Investigation of the nature and stability of the Martian seasonal water cycle with a general circulation model, *J. Geophys. Res.*, *107*(E5), 5031, doi:10.1029/2001JE001536.

Smith, M. D. (2004), Interannual variability in TES atmospheric observations of Mars during 1999–2003, *Icarus*, *167*, 148–165.

Toigo, A. D., M. I. Richardson, R. J. Wilson, H. Wang, and A. P. Ingersoll (2002), A first look at dust lifting and dust storms near the south pole of Mars with a mesoscale model, *J. Geophys. Res.*, *107*(E7), 5050, doi:10.1029/2001JE001592.

Toigo, A. D., M. I. Richardson, S. P. Ewald, and P. J. Gierasch (2003), Numerical simulation of Martian dust devils, *J. Geophys. Res.*, *108*(E6), 5047, doi:10.1029/2002JE002002.

Tyler, D., Jr., J. R. Barnes, and R. M. Haberle (2002), Simulation of surface meteorology at the Pathfinder and VL1 sites using a Mars mesoscale model, *J. Geophys. Res.*, *107*(E4), 5018, doi:10.1029/2001JE001618.

Tyler, D., Jr., S. C. R. Rafkin, A. D. Toigo, and T. Siili (2003), First steps towards a true intercomparison of Mars mesoscale models, paper presented at the International Workshop: Mars Atmosphere Modeling and Observations, Cent. Natl. d'Etud. Spatiales, Granada, Spain, 13–15 Jan.

Wang, H., and A. P. Ingersoll (2002), Martian clouds observed by Mars Global Surveyor Mars Orbiter Camera, *J. Geophys. Res.*, *107*(E10), 5078, doi:10.1029/2001JE001815.

Wilson, R. J., and K. Hamilton (1996), Comprehensive model simulations of thermal tides in the Martian atmosphere, *J. Atmos. Sci.*, *53*, 1290–1326.

Zurek, R. W., and R. M. Haberle (1988), Zonally symmetric response to atmospheric tidal forcing in the dusty Martian atmosphere, *J. Atmos. Sci.*, *45*, 2469–2485.

J. R. Barnes and D. Tyler Jr., College of Oceanic and Atmospheric Sciences, Oregon State University, 104 COAS Administrative Building, Corvallis, OR 97331, USA. (dtyler@coas.oregonstate.edu)